OCS Study
MMS 2007-022

Full-Water Column Current Observations in the Central Gulf of Mexico

Final Report

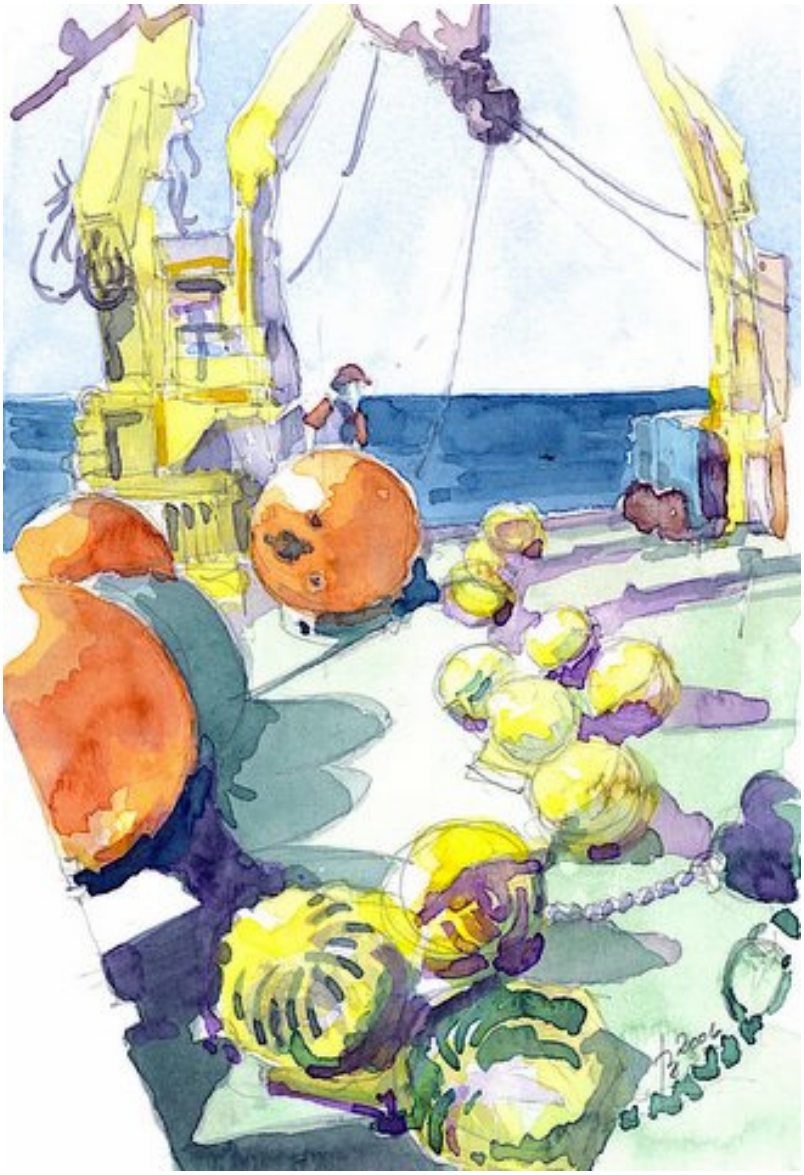

MMS U.S. Department of the Interior
Minerals Management Service
Gulf of Mexico OCS Region

OCS Study
MMS 2007-022

Full-Water Column Current Observations in the Central Gulf of Mexico

Final Report

Authors

J. Sheinbaum
A. Badan
J. Ochoa
J. Candela
D. Rivas
J.I. González

Prepared under MMS Contract
1435-01-02-CT-85309 (M02PC00008)
by
Centro de Investigación Científica
Y Educación Superior de Ensenada
Ensenada, Mexico

Published by

U.S. Department of the Interior
Minerals Management Service
Gulf of Mexico OCS Region

New Orleans
August 2007

DISCLAIMER

This report was prepared under contract between the Minerals Management Service and the Centro de Investigación Científica y Educación Superior de Ensenada (CICESE). This report has been technically reviewed by the MMS, and it has been approved for publication. Approval does not signify that the contents necessarily reflect the views and policies of the MMS, nor does mention of trade names or commercial products constitute endorsement or recommendation for use. It is however, exempt from review and compliance with the MMS editorial standards.

REPORT AVAILABILITY

Extra copies of this report may be obtained from the Public Information Office (Mail Stop 5034) at the following address:

U.S. Department of the Interior
Minerals Management Service
Gulf of Mexico OCS Region
Public Information Office (MS 5034)
1201 Elmwood Park Boulevard
New Orleans, Louisiana, 70123-2394

Telephone Number: 1-504-736-2519 or
1-800-200-GULF

CITATION

Suggested citation:

Sheinbaum J., A. Badan, J. Ochoa, J. Candela, D. Rivas, and J.I. González. 2007. Full water column current observations in the central Gulf of Mexico. U.S. Dept. of the Interior, Minerals Management Service, Gulf of Mexico OCS Region, New Orleans, LA. OCS Study MMS 2007-022. xiv + 58 pp.

ABOUT THE COVER

Canekito's mooring on the deck of UNAM's R/V *Justo Sierra*. Watercolor by A. Badan.

ACKNOWLEDGMENT

Thanks are due to Drs. Alexis Lugo-Fernández, MMS, and Van Waddell, SAIC, for their generous guidance throughout the development of the study, and to the captain and crew of the R/V *Justo Sierra* for their enthusiastic support at sea. We also thank the ample participation of CICESE's technical staff and students, in particular A. Ledo, M. Ojeda, B. Pérez, J. García, and C. Flores.

J. Sheinbaum
A. Badan
J. Ochoa
J. Candela
D. Rivas
and
J. I. González

TABLE OF CONTENTS

LIST OF FIGURES

LIST OF TABLES

ABSTRACT

A full-water column mooring, instrumented with acoustic current profilers, current meters, and temperature and pressure sensors, was installed at 25º 5'N; 90º 30'W, in the central Gulf of Mexico. It successfully monitored current and temperature fluctuations from the near surface to the bottom from May, 2003 to August, 2004 (16 months). The velocity spectral density shows peaks at tidal and inertial bands with over 90% of the variance in subinertial motions. Bursts of inertial wave activity occur throughout the period of observations, possibly related to the passage of eddy-related fronts. A considerable portion of the subinertial current fluctuations are surface intensified, coherent throughout the water column, and geostrophically related to the sea surface slopes, as determined from satellite altimetry. The projection of the data shows that the barotropic and first baroclinic dynamical modes contribute 46% and 45% of the total variance. An EOF decomposition shows 49% and 24% of the variance in the first and second modes, both of them exhibiting the surface intensification. An intensification detected within the bottom boundary layer probably arises as an effect of bottom-trapped topographic waves. Most of the fluctuations are driven by eddies propagating to the west, away from their generation off the Loop Current. The temperature measurements combined with the measured vertical excursions of some instruments and the dynamical modes allow estimates of the full temperature and vertical displacement profiles. Temperature fluctuations are consistent with the passage of warm/cold anticyclonic/cyclonic eddies.

1. Introduction

The Gulf of Mexico is the focus of a great deal of research because of its considerable strategic importance, which includes its geographical location, and the vast resources it contains. The Gulf includes the Exclusive Economic Zones (EEZ) of three nations (Cuba, México and the United States), and a portion of international waters. The U.S. has deployed considerable efforts to understand the circulation of the northern shelf and slope (e.g. Nowlin et al., 2000), adjacent to the Texas and Louisiana shelves, where considerable mineral reserves are known to exist. The territorial waters of Mexico remain much less explored, but their circulation is, of course, intimately linked to that of the rest of the Gulf. Basin-wide gyres and recirculations occupy the Gulf, eddies shed from the Loop Current propagate to the west and dissipate on Mexican shores, as do the Topographic Rossby Waves induced from the interactions of the Loop Current with the West Florida shelf (Hamilton, 1990; Hamilton and Lugo-Fernández, 2001). As the Minerals Management Service (MMS) of the U.S. Department of the Interior was embarking on an effort to refine the knowledge of the circulation over the northern slope, the authors thought it important to monitor currents concurrently just south of the main U.S. deployment, in order to provide a southward extension of the observations, and a much wider framework for our observations of the currents within the Mexican EEZ. The position chosen for our Canekito mooring was 25º05.4'N; 90º30.0'W, in 3590 m of water (Figure 1), thereby also providing measurements in the deepest portion of the Gulf that connects the eastern and western basins. There are no long-term series of observations available for this region and the impact of eddies and waves on its dynamics, particularly in the deepest part of the water column were unknown.

2. Setting and Data Characteristics

The subsurface mooring deployed for Canekito was designed to adequately sample the distribution of currents form the surface to the bottom, in the very deep waters of the central Gulf of Mexico. It supported two upward-looking 75 kHz RDI acoustic Doppler current profilers (ADCP's) programmed with 10 m bins. One of them was deployed at 335 m depth and reaching the surface, to document the increased energy levels in the upper layers, and the other at 1194 m, sampling up to 750 m below the surface, to measure currents in an intermediate transition layer supposed to exist around 1000 m depth. Observations from a mooring deployed earlier by Louisiana State University farther to the northeast (Welsh, pers. comm.) suggested the intermediate transition layer. A third, 300 kHz RDI ADCP, programmed with 8 m bins, was deployed at a depth of 3578 m, 12 m off the bottom and looking upwards, to document current fluctuations as close to the bottom as possible. Six Aanderaa RCM11 current meters were located between the ADCP's to sample current properties at intermediate levels (Figure 1). In this fashion, the water column was sampled from the surface to the bottom, save for the levels of acoustic interference that typically render the signal useless near the boundaries. All the instruments appear to have performed satisfactorily, except the intermediate ADCP near 1200 m depth, which inexplicably shows unrealistic data values and abnormally low variance levels in the 8 bins closest to the instrument's head; so we discard those few series of data.

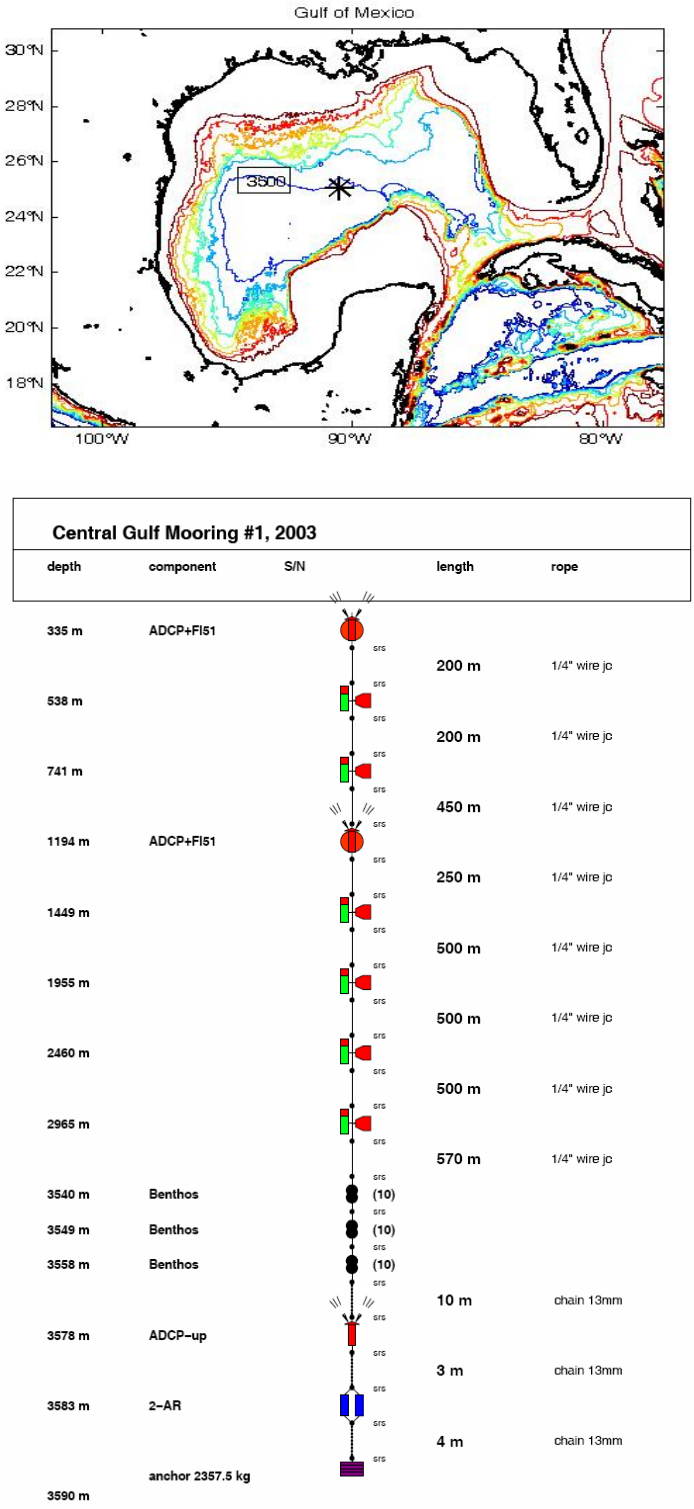

Figure 1. (a) Location of the Canekito mooring in the Central Gulf of Mexico (Contour interval is 500 meters. The star indicates the position of the mooring.) (b) Vertical distribution of instruments on the mooring.

Table 1 summarizes the basic setup and specifications of the two Long-Ranger ADCPs (LR1 and LR2) used in the mooring. Figure 2 depicts some performance statistics of these instruments. ADCPs perform four tests on velocity data, which are based on the comparison of the quality indicators of the records (correlation, echo intensity, error velocity, and percentage of good data) to the internal thresholds, defined during the instrument's programming. Records with less than 64 correlation counts, 50 echo intensity counts, 25 percent good, or those whose vertical velocities exceed 2000 mm/s are excluded. Details on the data quality tests and the internal thresholds can be found in RDI (1998) and on the RDI website (www.rdinstruments.com).

Table 1

Some Specifications of the ADCPs Used in this Study

	LR1	LR2
Position	25°05.15′N 90°30.00′W	
Water depth	3590 m	
Instrument depth	360.6 m	1226.9 m
ADCP type	RDI Workhorse Long Ranger / 76.8 kHz	
Filter mode	Broadband	
Serial number	3551	3452
Record length	2003/05/11/22:45:00 - 2004/08/27/21:15:00	
Number of data points	22,750 by depth bin	
Beam inclination	20°	
Pings per ensemble	18	
Seconds per ping	100	
Ensemble interval	1800 s	
Pulse/depth cell length	10 m	
First depth cell	17.98 m above head ($z = 342.6$ m)	18.56 m above head ($z = 1208.4$ m)
Nominal range	42 depth bins	50 depth bins
Useful data range	depth bins 2-31 ($z = 332.6$-42.6 m)	depth bins 7-48 ($z = 1148.4$-738.4 m)
Compass accuracy	±2°	
Tilt sensor accuracy	±0.5°	
Velocity accuracy	±5 mm s^{-1}	
Temperature precision	±0.4°C	

The quality indicators in our ADCP records were well above the excluding thresholds mentioned above. Indeed, their percentage of good velocity estimates (PG4), i.e. the velocity estimates obtained from the four beam solution, is astonishingly high in both instruments, with PG4 > 90%. Also, both the echo intensity and the correlation are above 80% in LR1 and above 95% in LR2. Nonetheless, only those data from bins 2 to 31 (from 333 m to 43 m depth) in LR1 and from bins 7 to 48 (from 1148 m to 738 m depth) in LR2 were retained.

In LR1, the four near-surface data (bins from 32 to 35, above 43 m depth) were too noisy to process, a consequence of a side lobe contamination from surface reflection (Schott, 1986; Schott and Johns, 1987; Flagg and Smith, 1989). The lowest bin is characterized by

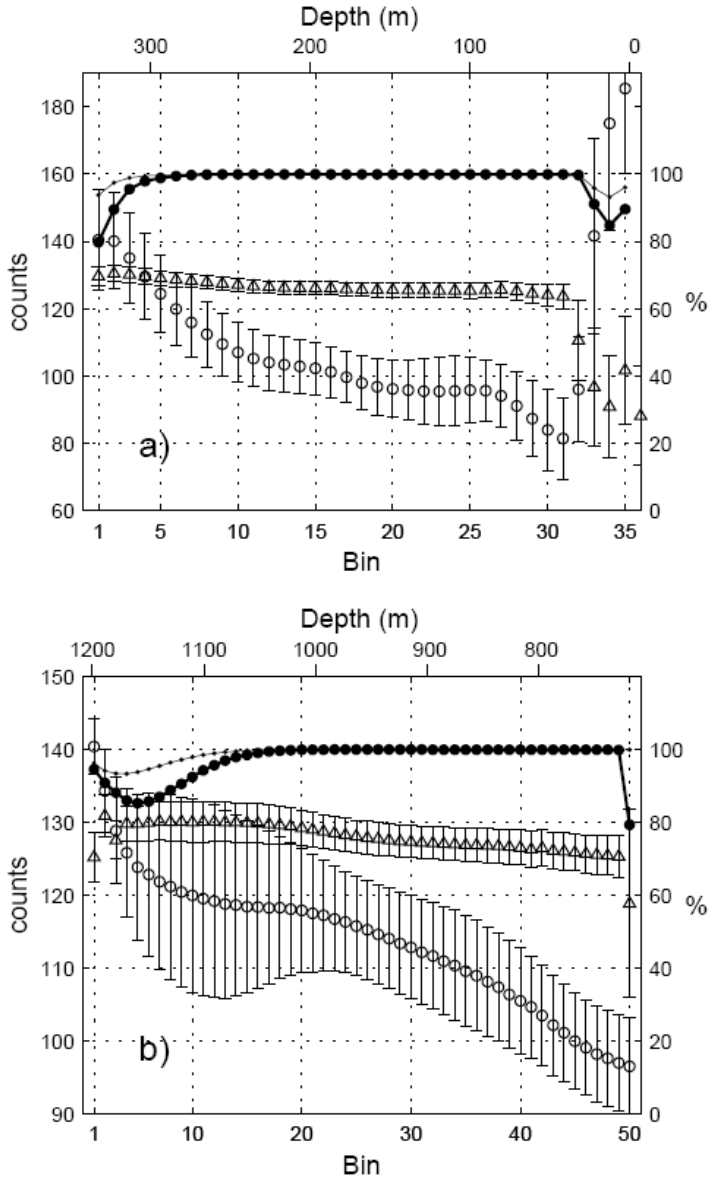

Figure 2. Mean values of some data quality indicators for LR1 (a) and LR2 (b). Left-side scale: White circles correspond to echo intensity; triangles correspond to four-beam averaged conditions; errors bars in both series indicate their standard deviation. Right-scale side scale: Black circles correspond to the percentage good data per ensemble for velocity components estimated from four beams (*PG*4); dots correspond to the percentage of data estimated from either three or four beams.

PG4 < 90%, and high enough values of both echo intensity and correlation, but shows no coherence with the bins immediately above.

In LR2, the lowest eight bins were rejected since they show unrealistic velocity signals, abnormally low variance and no coherence with series from bins above. Bad data from the first bins is an issue that has been reported previously (Schott 1988; Lohrmann et al., 1990; van Haren et al., 1994), but lacks a comprehensive explanation. For example: Flagg and Smith (1989) attribute this phenomenon to a ``residual transducer ringing", but do not elaborate; Chereskin et al. (1989) reports a bias that occurs in regions of high current shear, when the signal processing filter is not centered on the spectrum of the Doppler-shifted signal. Another possible explanation for this behavior is interference with the mooring cable. Notice (Fig 2 lower panel) that the highest bin also showed noisy data and relatively low PG4 (80%), slightly smaller correlation, but adequate echo intensity.

To better identify these problems in the actual profile, Figure 3 shows the mean and standard deviation vertical profile of the current speed. Red dots indicate actual measurements; green dots pinpoint data that will be used in an EOF analysis below. The anomalous measurements of LR2's near-head bins around 1000 m depth can be clearly seen as well as the last bins from the same instrument which show slightly larger variance than the nearby data.

Another source of potential problems with ADCP measurements can be large values of instrument tilt, since they can change the accuracy of both the compass and the tilt sensor, thus producing errors that can cause biased velocity records. RDI recommends (in the RDI's technical documentation available in www.rdinstruments.com) a maximum tilt of 15 degrees in order to maintain the accuracy of both the compass and the tilt sensor specified in Table 1. Fortunately, the tilt of both LR1 and LR2 never exceeded 5 degrees; indeed, the tilt was generally small: $1.7 \pm .1$ in LR1 and $1.2 \pm .6$ in LR2.

Both ADCPs had pressure sensors whose data show vertical excursions of the mooring. These data and their impact on temperature and velocity estimates are discussed below in the data analysis Section.

Besides the two Long-Rangers, there were six Aanderaa RCM11 acoustic current meters distributed along the water column (538, 741, 1449, 1955, 2460 and 2965 meters depth respectively, see Figure 1.B). Sampling interval was one hour and they also provide temperature data. The instruments were programmed considering the mean temperature at their corresponding deployment depth. For a consistency check, Figure 4 shows time series of low-pass filtered velocity components from one Aanderaa current meter and two neighboring bins of the LR2 ADCP at a depth of approximately 740 meters. The high visual agreement between both data gives one confidence in both measurements. Also, the rms of the difference in velocity, without any filtering, of contiguous bins in the LR2 measuring around 760 m depth is 7 cm/s while the difference of the Aanderaa velocity measurement with the velocity measured for the same depth (740 m) by the LR2 is 5 cm/s.

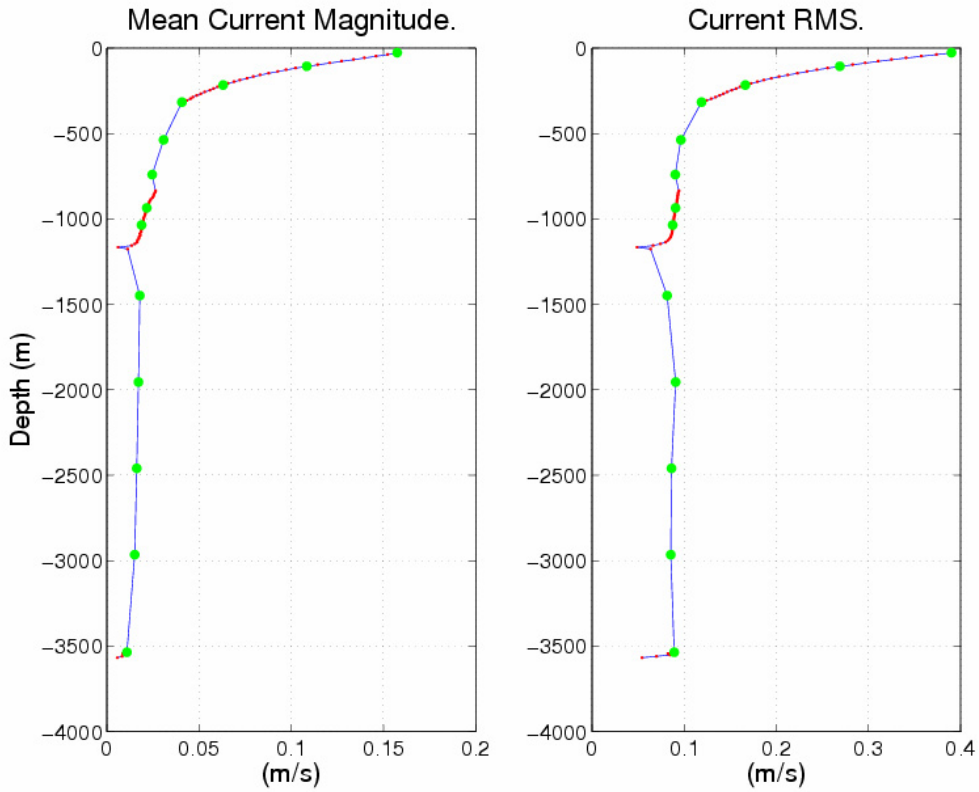

Figure 3. Magnitude of mean current (left panel) and current rms (right panel) vertical profiles from the Central Gulf mooring. The red dots indicate actual measured locations while the superposed large green dots indicate the measurements used in the EOF calculations discussed in Section 3.2. The figure visually highlights there are problems with the first bins of Long-Ranger LR2 instrument located at a nominal depth of 1240 m.

The deepest instrument in the mooring is a 300kHz up-ward looking Work Horse ADCP located about 12 m above the bottom. The instrument was programmed with a bin length of 8 m and was deployed to better resolve the bottom boundary layer. However, only the first 5 bins provided good quality continuous data. The other bins only provide sporadic measurements, due to low echo intensity. Data from the first bins was correlated with data from the rejected bins (when available) which indicates the instrument did not have the problems of the LR2 instrument reported above.

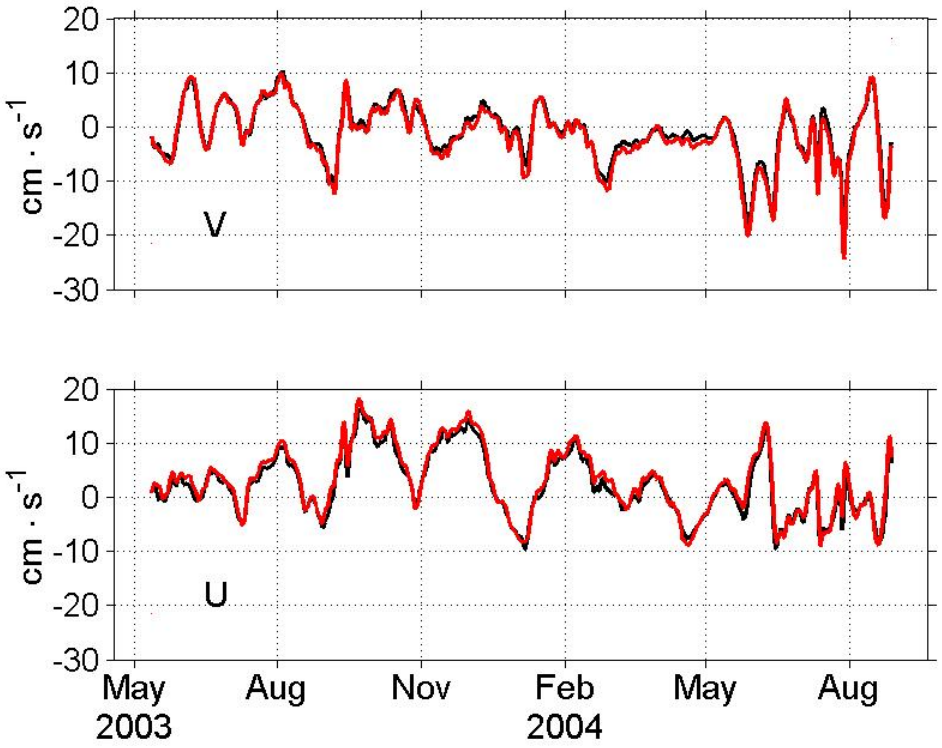

Figure 4. Comparison between the low frequency (subinertial) horizontal velocity components measured at the nominal depth of 740 m with the LR2 ADCP (black) and the Aanderaa Current meter (red).

Additional information obtained for this experiment consists of two full-water column CTD casts, one made prior to deployment and the other immediately after recovery, which provide reference profiles of the local hydrographic conditions surrounding the mooring. They are discussed in Section 4, where time-series of vertical temperature profiles from mooring measurements are computed. However, it is interesting to put these measurements in the context of other available observations in the region. Figure 5 shows a map of the available hydrographic stations in the NODC data bank in the Gulf. One can see most of them are concentrated in the northern Gulf of Mexico, with very few observations in its central and southern part. In fact only two full column CTD stations are available in the NODC data that are sufficiently close to the mooring. Figure 6 shows hydrographic NODC station data for the central Gulf of Mexico and Loop Current waters in the eastern part. Well-known differences between these profiles are clearly identified: for example, the subsurface salinity maximum of Loop Current waters, whose origin can be traced back to subtropical Atlantic waters, is clearly diminished and modified in the Gulf of Mexico waters. Waters above 1000 m in the Loop Current are in general warmer than Gulf of Mexico waters although this varies during the year; in fact, sea surface temperatures in both regions are very similar during summer. As we will see below, our hydrographic profiles are not much different from the ones shown in Figure 6.

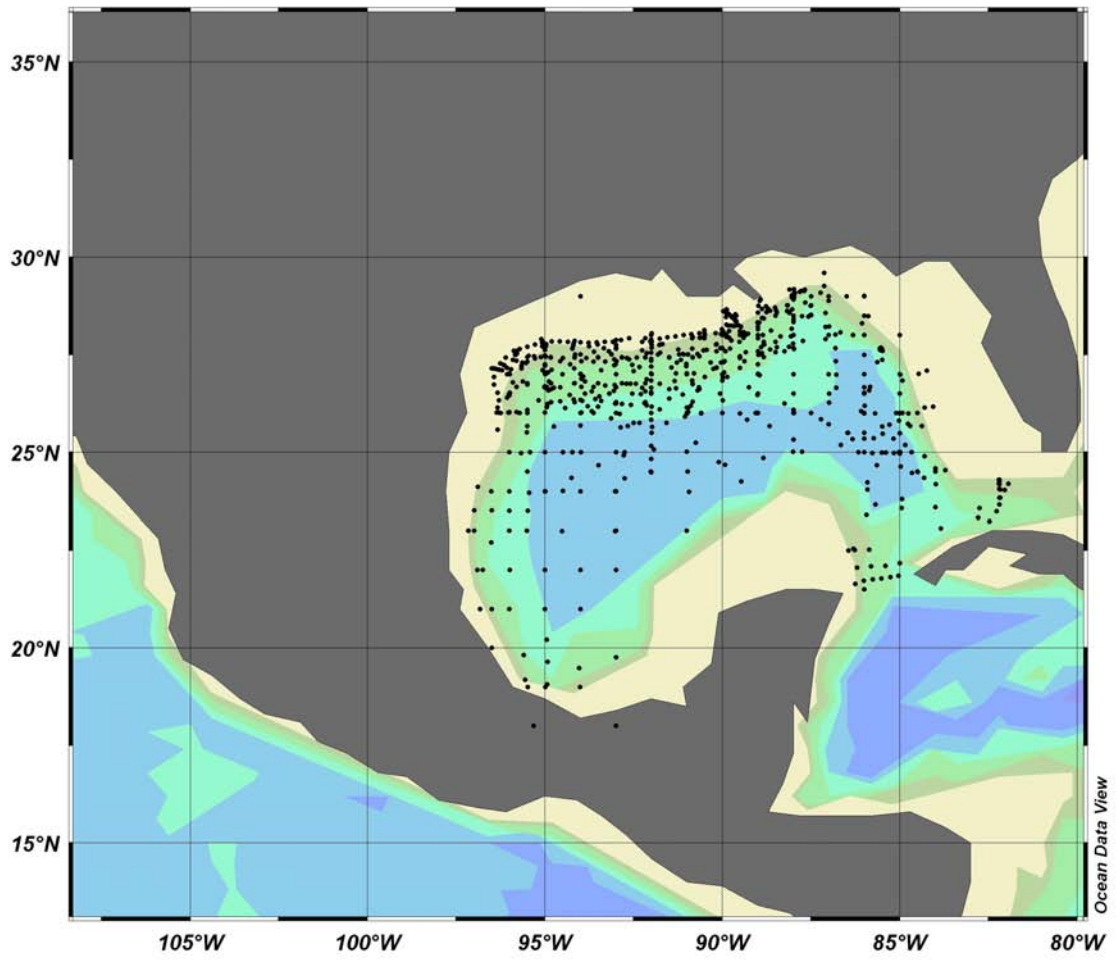

Figure 5. NODC hydrographic stations in the Gulf of Mexico.

Other important properties and differences between Gulf and Loop Current waters can be determined by looking at the vertical distributions of oxygen shown in Figure 7. The surface values are close to 4 ml/lt. An O2 minimum is found near 400 m depth, followed by an oxycline which starts at the level of the Florida sill. The concentration of dissolved oxygen increases monotonically with depth until it starts inflecting at the level of the deeper Yucatan sill (Rivas et al., 2005). From that level, it increases more slowly, but significantly, to attain its maximum values near the bottom at 3700 m depth. Subsurface minima and deep maximum values are not as extreme as in the Caribbean/ Loop Current values. Though relatively diminished, high deep oxygen values in the Gulf are indicative of ventilation by overflowing events at the Yucatan sill. The consequences of these processes have been discussed extensively in Rivas et al. (2005).

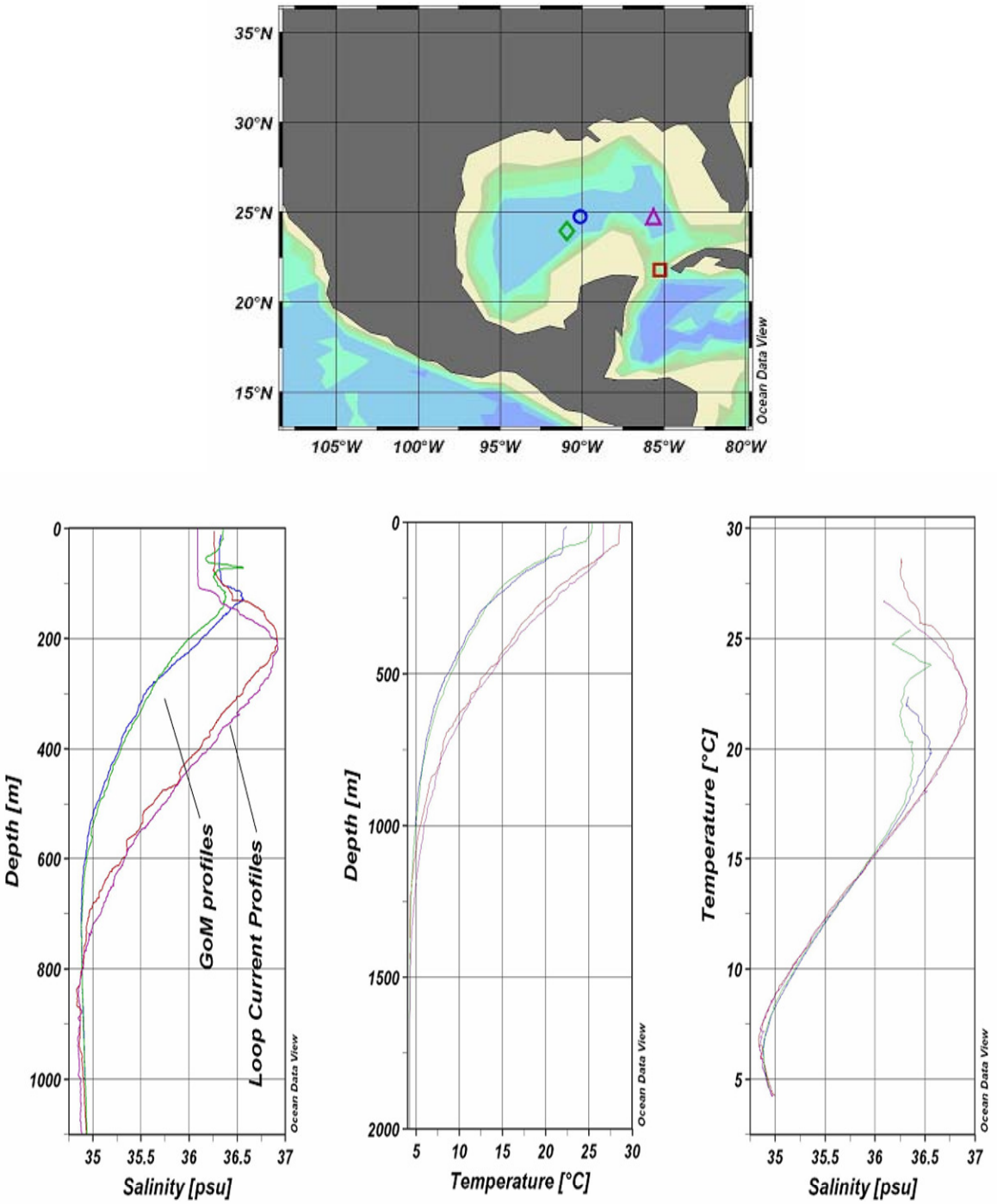

Figure 6. Vertical profiles of 4 NODC hydrographic stations, two in the Central Gulf of Mexico and two in the Loop Current region. Notice the difference between the two regions, quite clear from 1000 m depth to the surface.

Finally, satellite altimetry data will be extensively used for comparison and interpretation of the mooring velocity data since they allow clear identification of Loop Current extension and eddy events. Data comes from the AVISO gridded analysis.

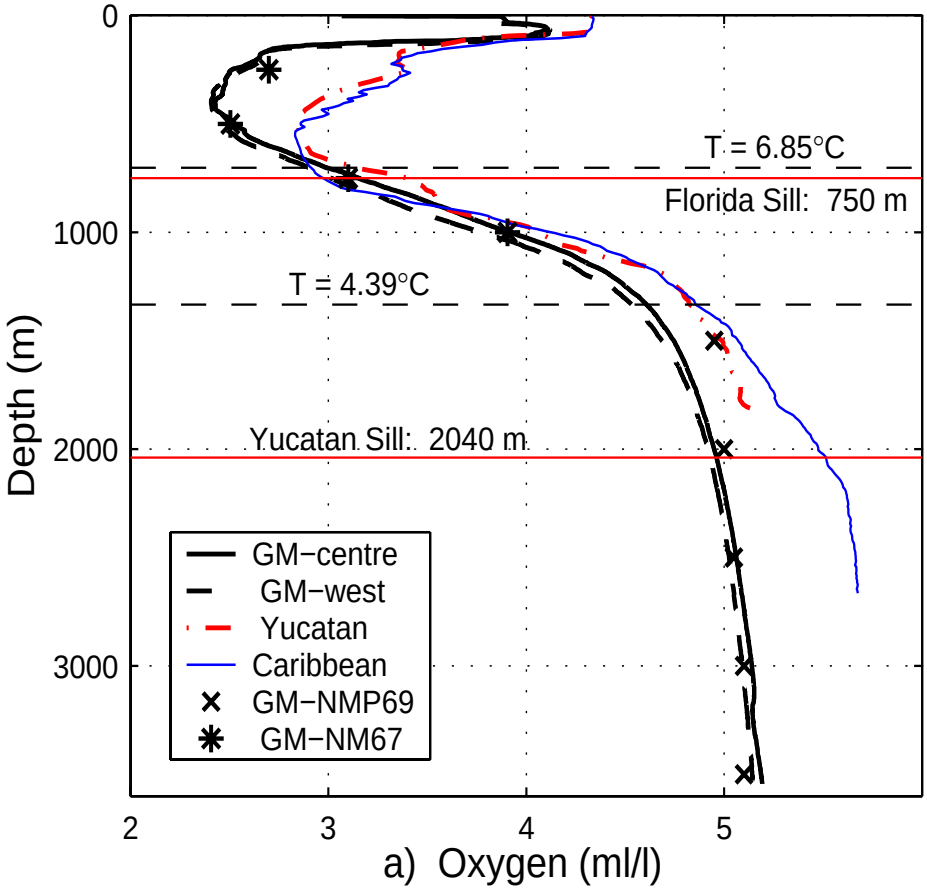

Figure 7. Vertical distribution of oxygen at various relevant locations in the Gulf of Mexico and in the Caribbean Sea. Asterisks and crosses indicate historical values reported for the central Gulf by Nowlin and McLellaan (1967) and Nowlin et al. (1969).

3. Data Analysis

3.1. Spectra

All instruments on the mooring recorded current and temperature data successfully for the duration of the deployment. The first step to understand the nature of velocity fluctuation is to analyze their spectral composition. Figure 8, panels a and b, shows spectra for the zonal and meridional velocity components at different depths. Panel c shows variance conserving spectra for the meridional velocity. These spectra were calculated with the multitaper Thomson method.

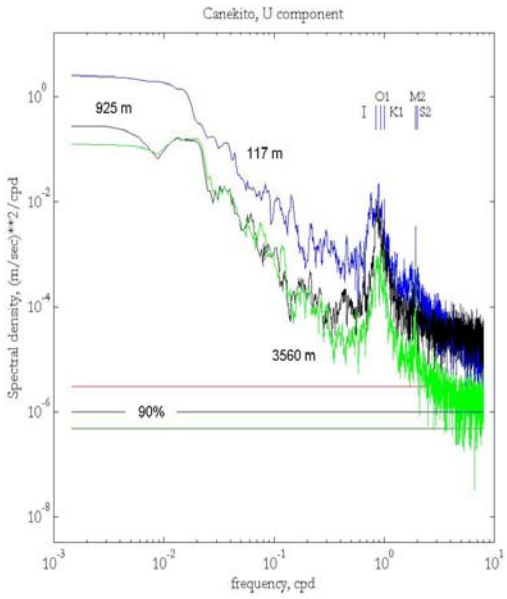

(a)

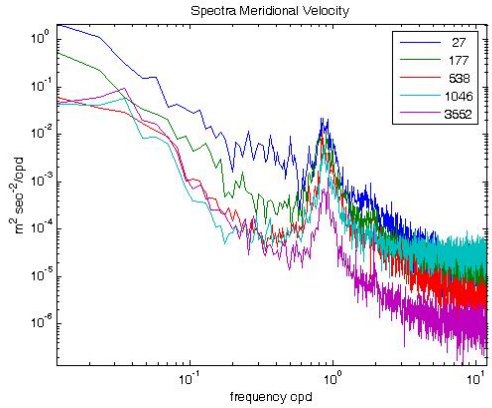

(b)

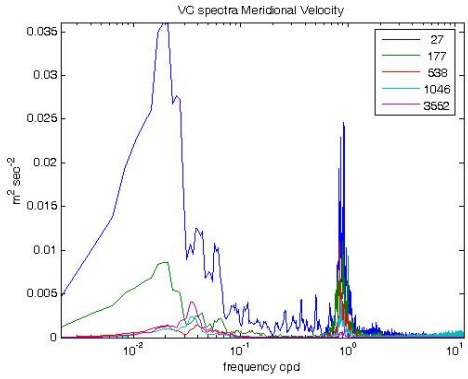

(c)

Figure 8. Spectra at different depths of the (a) zonal velocity, (b) meridional velocity. Panel (c) shows variance conserving spectra for meridional velocity to better identify spectral peaks.

Diurnal tides and inertial motions are clear signals with periods close to 1 day (inertial period at 25N is 1.18 days); they are clearly more energetic than the semi-diurnal tidal components and a small contribution to the overall variability. At the end of Section 5 near-inertial motions and its possible sources are discussed. Spectra are obviously red though, so lower frequency variability dominates the energy spectrum; about 10% of the velocity variance is due to near-inertial and higher frequencies. Energy is surface intensified, and shows a broad peak centered on a 50 day period, reflecting variability in the 30-100 day band. Several peaks appear in the 5-30 day band (also surface intensified). It is interesting to note that the peak centered at 30 days is higher at the deepest level than at other depths except for the surface. In fact energy in the 5-30 day band is slightly higher at the bottom than at other levels below the surface. Based on previous studies (Hamilton, 1990, Oey and Lee, 2003) this bottom energy intensification might be associated with the presence of topographic Rossby waves, but further analysis is necessary. Comparison with altimetry observations (see Section 5) suggests the low frequency variability at 30 days and longer periods is related to the passage of eddies. There is energy at even lower frequencies, but a proper characterization of such motions in the central Gulf of Mexico would require maintaining a mooring for a longer period.

From here onwards, emphasis is put on subinertial frequency variability, (although we show a figure on near-inertial bursts in Section 5 below). To do that, velocity and temperature time-series were low-passed filtered with a Lanczos filter using a 48 hours half power point. This effectively filters tidal and inertial motion. Results refer to these low-pass time series unless stated otherwise.

Low-passed currents are found to be energetic and highly coherent throughout the water column, with many fluctuations traceable by eye from the surface to the bottom. Figure 9 shows time series of horizontal velocity vectors at different depths. The horizontal velocity vectors describe features typical of rotational perturbations, turning either clockwise or counterclockwise, suggesting the passage of eddies.

Many of these perturbations can be traced from the surface to the bottom, and are seen to cause the largest drag and tilting of the mooring (discussed below), despite their smaller amplitude. Other larger fluctuations are confined to the upper 500 m or so. Other events appear most intense at mid-water, especially towards the last four months of the data series, without an immediate clear explanation for such intensification. Beneath 1200 m, in the deeper layer, velocity fluctuations are remarkably coherent throughout the water column, with only a small intensification within the layers closest to the bottom. Dynamically, it appears that the water column can be divided into three layers, a surface layer above 500 m, under the direct influence of surface eddies and possibly wind influences, an intermediate layer (500-1200 m) with as yet unexplained intensification of its own, and a deeper layer (1200- bottom) which is strikingly coherent. In addition, a thin bottom boundary layer is detectable in the lowest few meters of the water column. Decomposition in dynamical vertical normal modes will show most of the energy is equipartitioned in the barotropic and first baroclinic modes.

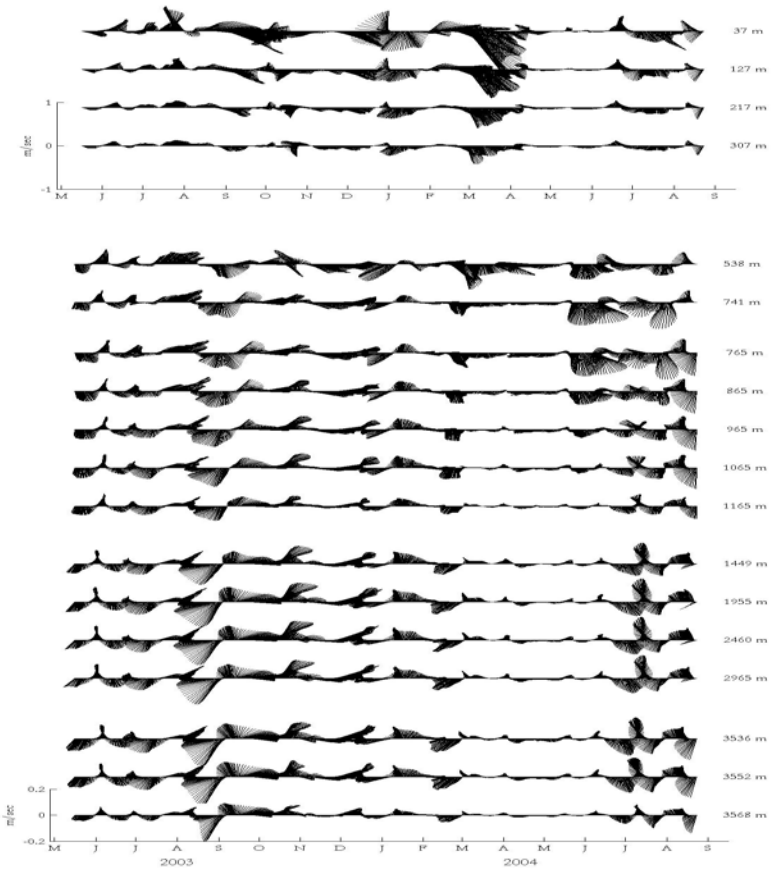

Figure 9. Vector diagrams of the velocity (North component up page, East component to the right) field at most levels at Canekito. The barotropicity of the signals is evident, as are surface events in the upper layers, and mid-water events during the last four months of the observation series.

As is common in most oceanographic measurements, the mean velocity is smaller than its standard deviation (Figure 10), here with mean currents flowing to the southeast at no more than 0.1 m sec^{-1} in the upper layer, and diminishing from there to only one or two cm.sec^{-1} near the bottom, following to the northeast. The standard deviation is closer to 25 cm sec^{-1} near the surface, with the principal axis of variance oriented in a northwest to southeast direction, diminishing rapidly with depth, to about 5 to 10 cm sec^{-1} throughout the water column.

Table 2 gives quantitative basic statistics of the low frequency velocity data.

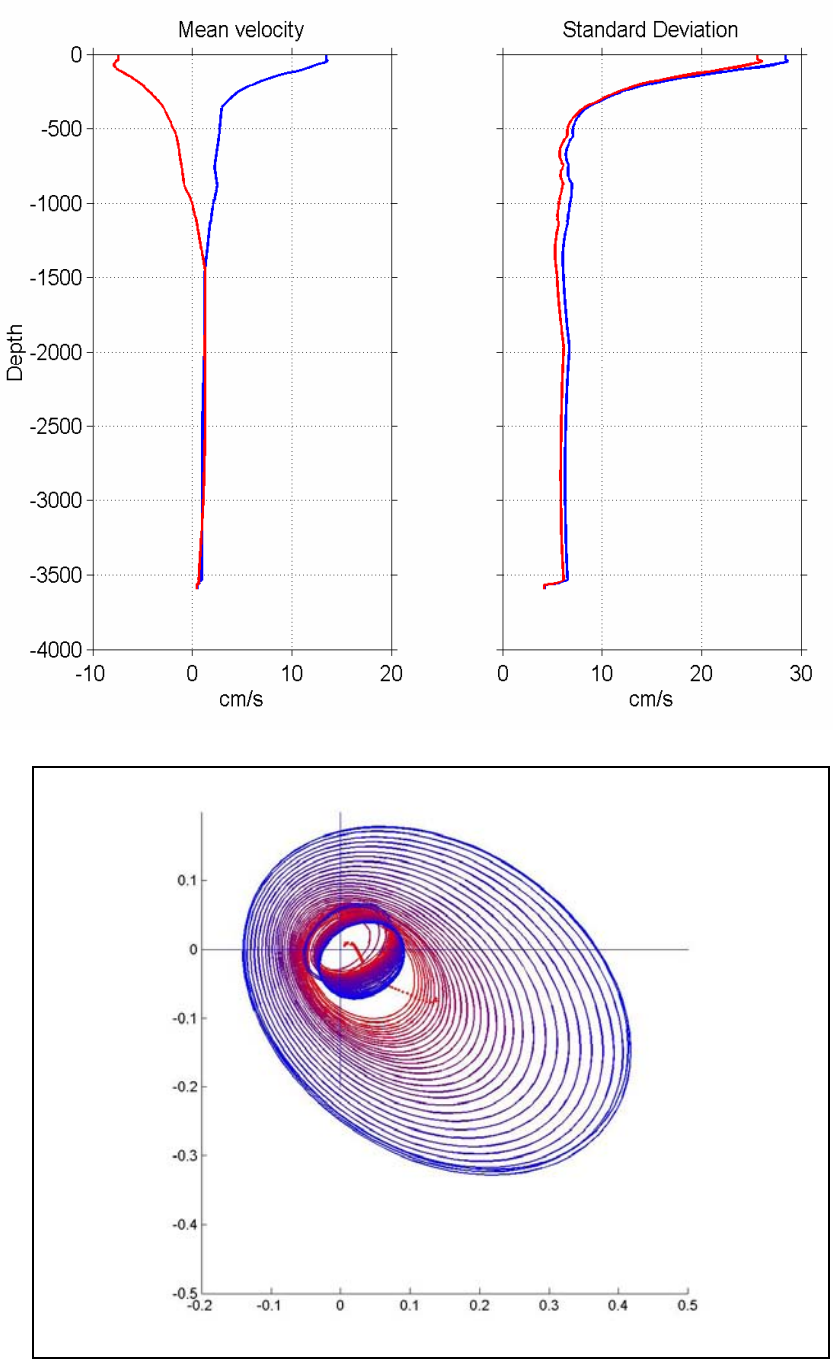

Figure 10. Distribution of the mean, standard deviation (4.a and 4.b, Eastward (blue), Northward (red)), and ellipse variance (4.c) with depth. The mean is largest near the surface and directed to the southeast down to 1000 m depth and to the northeast below that depth. The standard deviations are larger than the mean in the whole water column with maxima near the surface, with the principal axis oriented in a northwest to south east direction in the upper layers, and shifting to northeast to southwest direction mid-water and in the bottom boundary layer.

Table 2

Basic Statistics of Low-Passed Velocity Data

Depth	mean u	std u	min u	max u	mean v	std v	min v	max v
27	0.136	0.283	-0.595	1.107	-0.077	0.254	-1.309	0.581
37	0.130	0.271	-0.593	0.954	-0.077	0.244	-1.215	0.545
47	0.123	0.257	-0.599	0.846	-0.076	0.235	-1.121	0.531
57	0.117	0.244	-0.581	0.822	-0.074	0.225	-1.020	0.488
67	0.111	0.233	-0.559	0.813	-0.072	0.215	-0.934	0.418
77	0.105	0.221	-0.553	0.795	-0.069	0.205	-0.861	0.377
87	0.099	0.210	-0.511	0.781	-0.066	0.195	-0.817	0.338
97	0.093	0.200	-0.465	0.748	-0.064	0.185	-0.772	0.317
107	0.088	0.188	-0.442	0.700	-0.062	0.175	-0.700	0.296
117	0.082	0.178	-0.443	0.666	-0.059	0.166	-0.676	0.271
127	0.077	0.170	-0.432	0.657	-0.057	0.158	-0.649	0.248
137	0.073	0.162	-0.424	0.631	-0.055	0.151	-0.631	0.232
147	0.068	0.154	-0.409	0.589	-0.053	0.145	-0.612	0.226
157	0.064	0.147	-0.396	0.540	-0.051	0.138	-0.592	0.231
167	0.061	0.139	-0.383	0.497	-0.049	0.131	-0.572	0.209
177	0.058	0.133	-0.353	0.474	-0.047	0.125	-0.540	0.188
187	0.054	0.127	-0.333	0.461	-0.045	0.120	-0.530	0.180
197	0.051	0.121	-0.306	0.462	-0.044	0.116	-0.519	0.179
207	0.048	0.116	-0.288	0.454	-0.043	0.111	-0.521	0.169
217	0.045	0.111	-0.276	0.411	-0.041	0.107	-0.518	0.168
227	0.043	0.108	-0.275	0.398	-0.039	0.103	-0.513	0.174
237	0.042	0.105	-0.278	0.384	-0.038	0.100	-0.518	0.168
247	0.040	0.101	-0.273	0.360	-0.037	0.097	-0.511	0.165
257	0.038	0.096	-0.261	0.337	-0.035	0.093	-0.507	0.153
267	0.036	0.093	-0.273	0.327	-0.034	0.090	-0.506	0.142
277	0.035	0.091	-0.291	0.306	-0.032	0.088	-0.499	0.148
287	0.033	0.088	-0.280	0.283	-0.031	0.085	-0.494	0.148
297	0.032	0.084	-0.278	0.283	-0.030	0.082	-0.491	0.141
307	0.031	0.081	-0.258	0.281	-0.029	0.078	-0.486	0.128
317	0.029	0.077	-0.264	0.277	-0.027	0.074	-0.464	0.130
538	0.026	0.063	-0.138	0.172	-0.014	0.055	-0.211	0.121
741	0.022	0.058	-0.108	0.167	-0.010	0.052	-0.234	0.112
836	0.025	0.060	-0.103	0.165	-0.007	0.048	-0.168	0.122
846	0.025	0.060	-0.108	0.176	-0.006	0.047	-0.160	0.121
856	0.024	0.060	-0.108	0.173	-0.006	0.047	-0.154	0.120
866	0.024	0.060	-0.098	0.169	-0.005	0.047	-0.156	0.115

Table 2 Basic Statistics of Low-Passed Velocity Data (Continued)

876	0.024	0.060	-0.096	0.173	-0.005	0.047	-0.162	0.118
886	0.023	0.060	-0.098	0.178	-0.004	0.047	-0.159	0.124
896	0.023	0.060	-0.093	0.173	-0.003	0.046	-0.156	0.125
906	0.023	0.060	-0.095	0.172	-0.002	0.046	-0.154	0.122
916	0.022	0.060	-0.094	0.167	-0.001	0.046	-0.157	0.122
926	0.022	0.059	-0.096	0.166	-0.001	0.045	-0.150	0.114
936	0.021	0.060	-0.108	0.170	0.000	0.045	-0.148	0.110
946	0.021	0.060	-0.105	0.166	0.000	0.045	-0.160	0.110
956	0.021	0.060	-0.103	0.167	0.001	0.046	-0.143	0.113
966	0.021	0.060	-0.103	0.173	0.001	0.046	-0.143	0.114
976	0.021	0.060	-0.103	0.171	0.002	0.046	-0.136	0.113
986	0.020	0.060	-0.103	0.169	0.002	0.046	-0.144	0.115
996	0.020	0.060	-0.105	0.167	0.003	0.046	-0.145	0.110
1006	0.020	0.060	-0.112	0.168	0.003	0.046	-0.151	0.111
1016	0.020	0.059	-0.105	0.164	0.003	0.046	-0.134	0.110
1026	0.019	0.059	-0.103	0.166	0.004	0.046	-0.149	0.107
1036	0.019	0.059	-0.107	0.160	0.004	0.046	-0.149	0.102
1046	0.019	0.059	-0.110	0.156	0.004	0.047	-0.160	0.116
1056	0.019	0.058	-0.117	0.164	0.005	0.046	-0.149	0.116
1066	0.018	0.058	-0.117	0.161	0.006	0.047	-0.142	0.117
1076	0.018	0.058	-0.117	0.156	0.006	0.047	-0.139	0.112
1086	0.017	0.058	-0.120	0.152	0.006	0.047	-0.140	0.116
1096	0.017	0.057	-0.109	0.154	0.006	0.046	-0.145	0.110
1106	0.017	0.057	-0.124	0.149	0.006	0.046	-0.147	0.117
1116	0.017	0.057	-0.120	0.152	0.006	0.045	-0.143	0.118
1126	0.015	0.055	-0.113	0.159	0.007	0.045	-0.133	0.117
1136	0.015	0.053	-0.111	0.151	0.007	0.044	-0.130	0.120
1146	0.014	0.050	-0.107	0.143	0.007	0.040	-0.126	0.103
1156	0.013	0.044	-0.089	0.117	0.006	0.036	-0.115	0.094
1166	0.006	0.028	-0.060	0.079	0.003	0.027	-0.076	0.084
1176	0.008	0.035	-0.082	0.112	0.008	0.040	-0.081	0.109
1449	0.012	0.059	-0.143	0.166	0.015	0.051	-0.177	0.163
1955	0.012	0.066	-0.165	0.186	0.014	0.059	-0.209	0.176
2460	0.010	0.062	-0.167	0.163	0.015	0.057	-0.211	0.172
2965	0.010	0.062	-0.153	0.165	0.013	0.056	-0.226	0.175
3536	0.009	0.064	-0.144	0.157	0.008	0.058	-0.238	0.168
3544	0.007	0.058	-0.127	0.139	0.007	0.054	-0.234	0.151
3552	0.008	0.060	-0.144	0.148	0.009	0.056	-0.236	0.144
3560	0.006	0.049	-0.120	0.132	0.007	0.047	-0.232	0.118
3568	0.004	0.038	-0.093	0.117	0.005	0.036	-0.223	0.094

The coherent motion with depth also can be visualized using progressive vector diagrams (Figure 11). The top 700 meters are coherent and imply flow to the south-east. The middle layer's width is about 200 m and velocities are slightly to the north-east, turning to the south at the end of the measurement period. The bottom layer movement is also slightly to the north-east (bottom to 1500 m). It is surprising how coherent are the velocities in each of these layers.

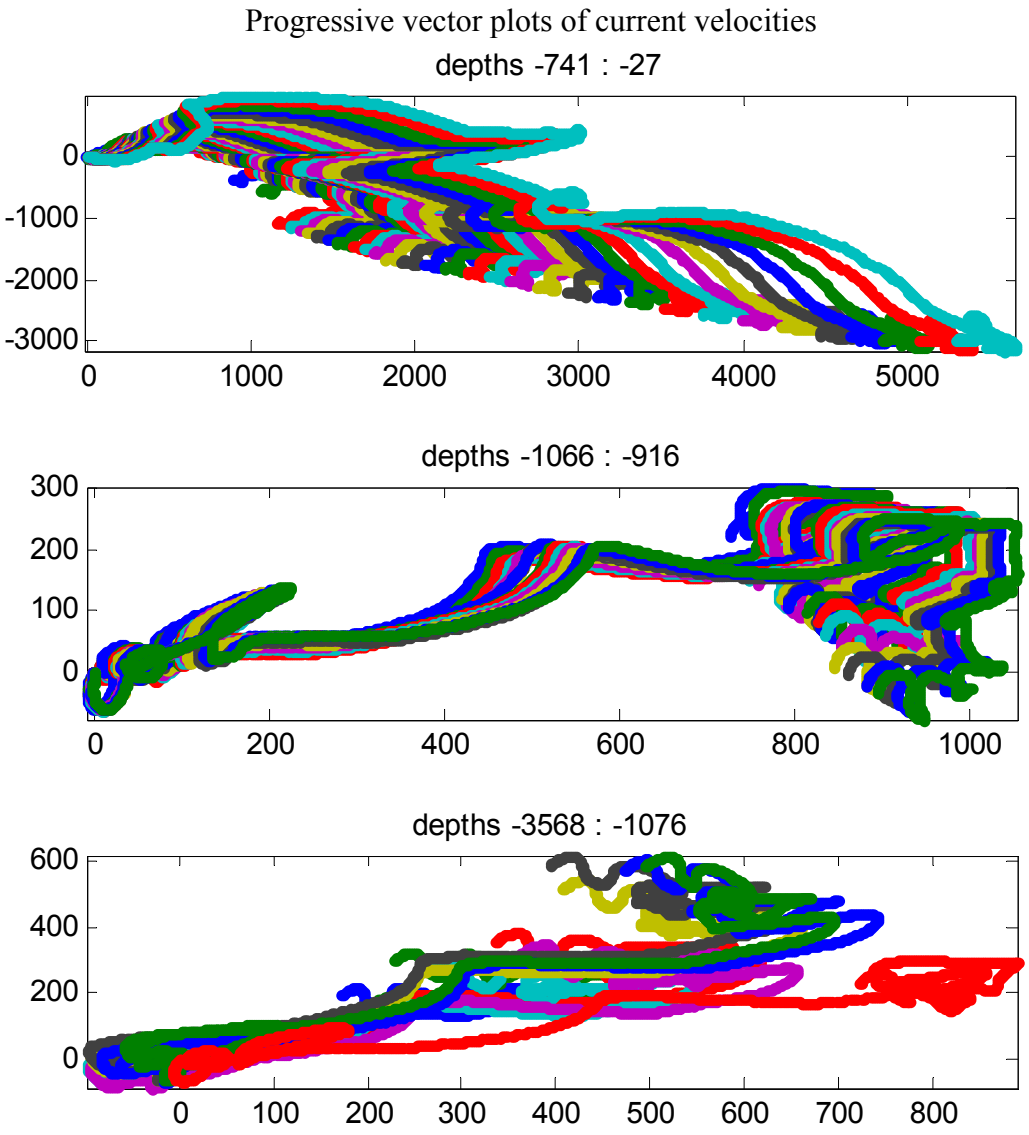

Figure 11. Progressive vector diagrams. Top 700 meters, a middle layer of 200 m width and the bottom layer show high coherence of the velocities in each of these layers.

3.2. Modal Decompositions

The velocity fluctuations or any other signal which is distributed throughout a region, such as the vertical water column, can be decomposed into 'modes' of variation, which group portions of the fluctuations that are, according to some convenient criterion, somehow coherent among the same mode and independent of the others (orthogonal in given metric). The full variance must be distributed among the different contributions of modes. The ruling criterion might be a purely statistical property of the data, or some underlying dynamical structure of physical significance. For example, according to the linearized governing dynamical equations proper for subinertial motions, a set of internal modes are deduced from the hydrographic distribution. In turn, each of these modes of variation, in particular the ones that most contribute to the variance, can (though not always) point to a cause of the motion. A set of modes that obey a statistical criteria are the Empirical Orthogonal Functions (EOF's).

3.2.1. Dynamical Modes

The expansion of velocity data in dynamical modes, for either u the eastward or v for northward components, uses a version of horizontal velocity modes, such that $u(z,t) = \alpha_0(t)U_0(z) + \alpha_1(t)U_1(z) + \ldots$, where the coefficients α_i $(i = 1,2,\ldots)$ hold the units (m s^{-1}). The set of modes U_i is orthonormal in the sense that $H^{-1}\int_{-H}^{0} U_k U_l dz$ is null, when $k \neq l$ or 1 when $k = l$ (H is the full depth of the column, 3750 m), whence $\alpha_i(t) = H^{-1}\int_{-H}^{0} u(z,t)U_i(z)dz$ and $H^{-1}\int_{-H}^{0} u^2(t)dz = \alpha_0^2(t) + \alpha_1^2(t) + \ldots$. The horizontal velocity modes (i.e. the set of *U's*) are derived from a numerical discretization of

$$F'' + \frac{N^2}{c^2}F = 0, \tag{1}$$

where, $F = F(z)$, $N^2(z) \equiv -\frac{g}{\overline{\rho}}\frac{d}{d}\frac{\overline{\rho}}{z}$, and $\overline{\rho} = \overline{\rho}(z)$ is the 'local' potential density. The boundary conditions are the rigid lid approximation and flat bottom (i.e. *F=0* at *z=0*, the surface, and *z=-H*, the bottom). The eigenvalues (i.e. *c's*) are the phase speeds, in the absence of rotation, of long gravity waves (see Table 3). The set of eigenfunctions proper for the horizontal velocities are not the eigenfunctions of Equation (1), but their derivative (i.e. *U=dF/dz*, see Figure 12 where the difference of the boundary condition in *U's* and *F's* is clear).

The measurements provide extensive, though not complete coverage of the water column. The depths where the velocity measurements are available are not fixed but, since pressure sensors are available at the three ADCP's, the depth estimation of each instrument is possible. The full profiles are estimated from the surface to the bottom every 10 m via plain linear interpolations where applicable, extrapolations to zero at the bottom, and a uniform extension to the surface. The modal expansion is done for the subinertial anomalies of velocity (i.e. the time mean and suprainertial fluctuations at each depth level are removed before the projection procedure). Mean and standard deviation profiles are shown in Figure 10. Without extrapolations, it is possible to truncate the vertical modes and the results are quantitatively very close and qualitatively the same. The same holds if the extrapolation to zero at the bottom is replaced by a uniform velocity from the deepest measurement to the bottom. The numerical modes are not

fully orthogonal, but the loss of orthogonality is small; the projections of the first seven modes into the others are smaller than 4% in magnitude. Figure 13 and Table 4 summarizes the spectral decomposition of the low-pass frequency variability. Nearly 90% of the variance is explained by the barotropic and first baroclinic modes with near equipartition of the energy. This results from both, the near surface intensification of the variability, and the strong coherence of the motion in the whole water column. The middle layer intensification of events towards the final part of the time-series seen in Figure 9 requires an unusually intense contribution from higher vertical modes. Table 4 partitions the variance contribution of each mode in terms of its principal axis and gives also its orientation. Figure 14, shows the amplitude of the barotropic and first baroclinic modes associated with principal axes of variability. One can clearly see that energy is equipartitioned between the modes and the periods when barotropic (baroclinic) signals dominate the variance.

Table 3

Mode Descriptive Parameters

MODE	Cn m/s	Cn/f Km	Depths of zero crossing M
Barotropic	200	3000	
1st Baroclinic (rigid lid approx.)	2	31.4	890
2	1.1	17.7	110, 1100
3	0.7	11.4	35, 355, 1300
4	0.5	8.4	25, 165, 550, 1450
5	0.4	6.6	20, 90, 310, 690, 1600

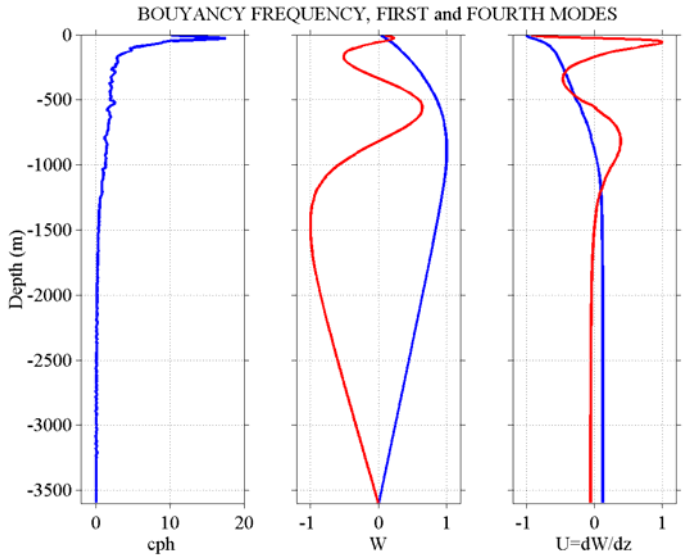

Figure 12. Dynamical internal modes as deduced from the hydrographic distribution (see text around Equation 1) in the Central Gulf of Mexico during Canekito. Vertical displacements and velocity component are in terms of modes in panel W, horizontal velocity modes are in panel U. Only the first (in blue) and the fourth (in red) internal modes are shown.

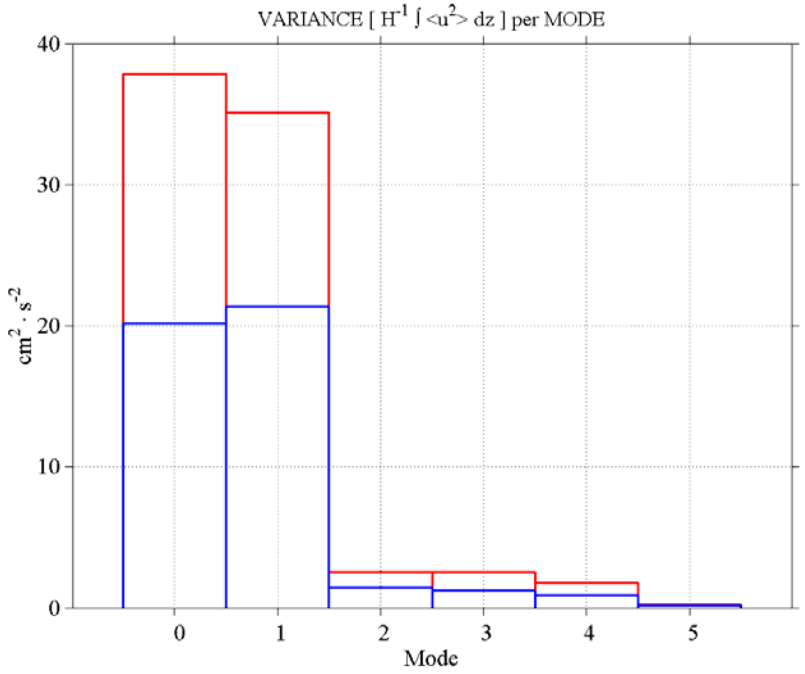

Figure 13. Spectra in terms of dynamical modes. In red is the variance in the semimajor axis and in blue in the semiminor. The total spectrum is the sum of both. The barotropic (0) and first baroclinic (1) modes account for nearly 90% of the total subinertial variance.

Table 4

Spectra and Characteristics of Modes

The total variance of the velocity is $H^{-1}\int_{-H}^{0} < u^2(t) > dz = < \alpha_0^2 > + < \alpha_1^2 > + ... = 130 cm^2 s^{-2}$, the orientation is counterclockwise, in degrees relative to the East.

MODE	Variance (cm/s)²	Major Axis % of Total Variance	Minor Axis % of Total Variance	Eccentricity	Ellipse Orientation
Barotropic	56.0	28	15	0.51	32
1st Baroclinic (rigid lid approx.)	58.9	29	17	0.50	-69
2	2.5	1.1	0.8	0.41	-33
3	4.0	2.1	1.0	0.56	-53
4	4.6	2.4	1.2	0.54	-69
5	0.7	0.3	0.2	0.36	-52

3.2.2. EOF

Another method to decompose the variance in 'orthogonal' patterns is the Empirical Orthogonal Function decomposition (EOF). This is a statistical method, which computes the eigenvectors or modes and associated eigenvalues (associated variance) of either the velocity vector covariance matrix or correlation matrix. When the covariance matrix is used, the eigenvectors are biased towards the region of higher variability (e.g. in this case, the surface). One way to obtain patterns that are not biased toward the highest variability regions is to use the normalized covariance matrix or correlation matrix. Both are discussed below. To avoid biasing the EOFs calculations, and account for the anomalous behavior of the ADCP at 1194 m (LR2, see Section 2), the observations from the ADCPs on the mooring were sub-sampled. It was decided to use only 4 levels from the upper most ADCP located a 335 m, 2 from the 1194 m instrument and only one from the deepest ADCP located at a nominal depth of 3578 m. A total of 13 measurements levels are used for the EOFs calculations, corresponding to the following depths: 27, 107, 217, 317, 538, 741, 936, 1036, 1449, 1955, 2460, 2965 and 3536 m, which are indicated by the large green dots on the panels of Figure 3.

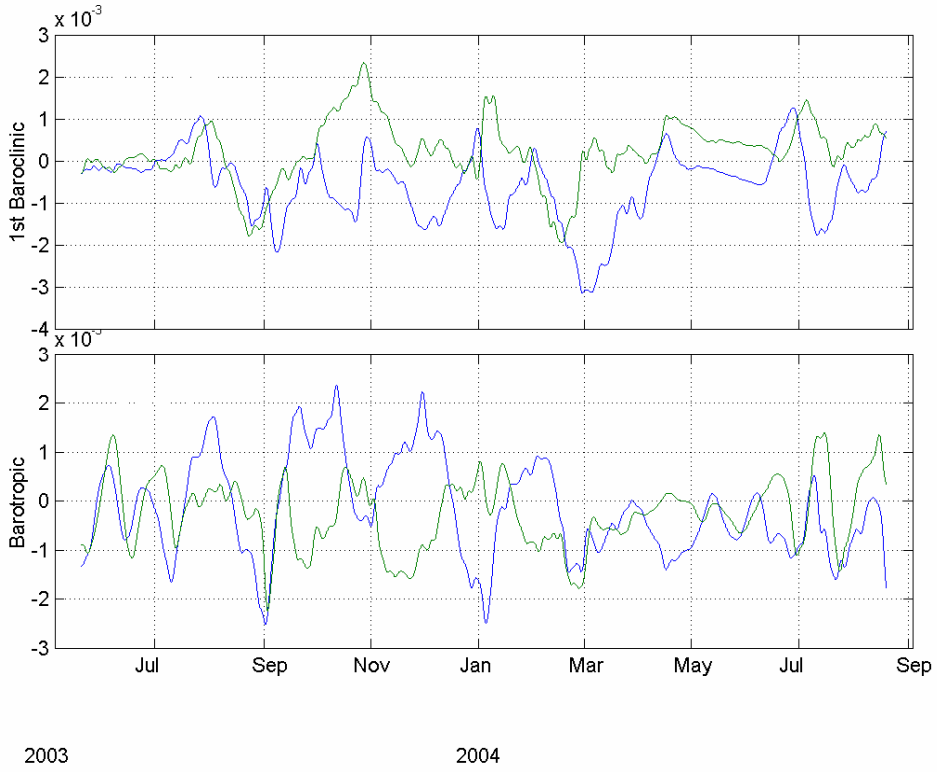

Figure 14. Amplitudes of barotropic and first baroclinic dynamical modes in the components of maximum variance (semi-major axis, blue) and minimum variance (semi-minor axis, green). The major axis of variability is at 32 degrees counterclockwise relative to East for the barotropic, and 70 degrees for the baroclinic (see Table 4).

The EOFs are calculated using the East (u) and North (v) current components at each level simultaneously, that is, by constructing a data matrix whose columns (or rows) consist of the time series of u and v at each level. With this arrangement, the spatial structure of each EOF mode is a frozen profile of velocity with a specific magnitude and orientation at each depth level and the principal components is the multiplicative factor that defines its time evolution. Both, the spatial structure and the principal component, are real numbers without the need to use complex EOF analysis.

The first 4 EOF modes of the total currents for the 13 vertical level chosen are shown in Figure 15 (a, b, c, and d). The first 2 modes, (Figures 15a, b), represent 73% of the observations variance and suggest a first baroclinic mode structure with a zero crossing at about 1200 m depth, with the current vectors of each mode corresponding to two principal axes of variability at each level. Modes 3 and 4 (Figures 15c, d) correspond to a nearly barotropic mode structure and account for only 17 % of the total variance. Table 5 gives the percentage of variance contained in the sub-inertial bands for the u and v components of the current.

Table 5

Percentage of Variance with Depth

Depth (m)	U % of lowpass variance	V % of lowpass variance
27	95	93
107	92	90
217	86	86
317	82	82
538	77	73
741	76	73
936	74	63
1036	77	69
1449	94	92
1955	96	96
2460	96	97
2965	96	96
3536	94	94

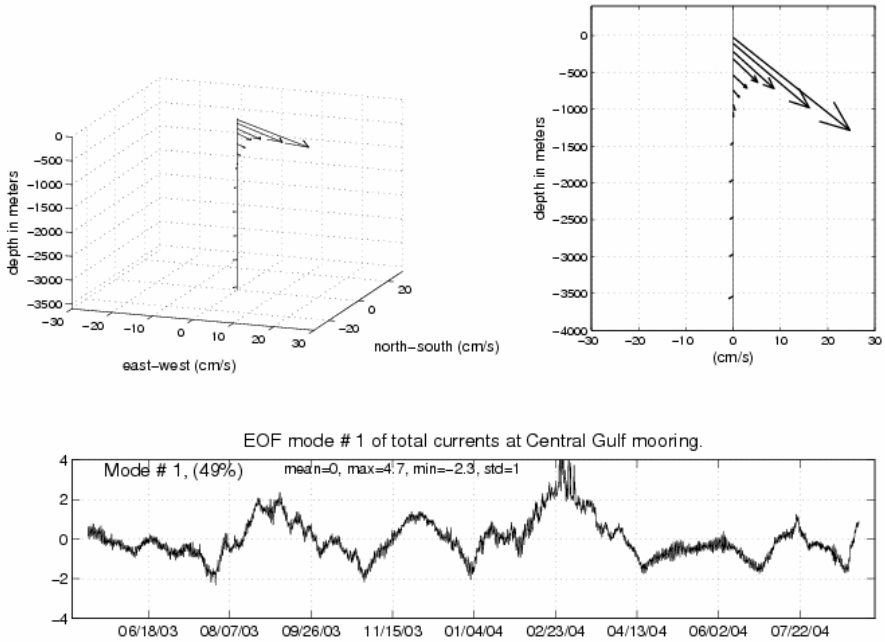

Figure 15a. EOF mode 1 for the total current observed at the 13 chosen vertical levels. The upper two panels show the dimensioned spatial structure of the mode in two equivalent representations, on the left, vectors in 3-D space, and on the right, vectors in 2-D with the north-south/east-west component in the abscissa/ordinate directions and each vector starting at its corresponding depth. The lower panel shows the time series (also called principal component) of the mode.

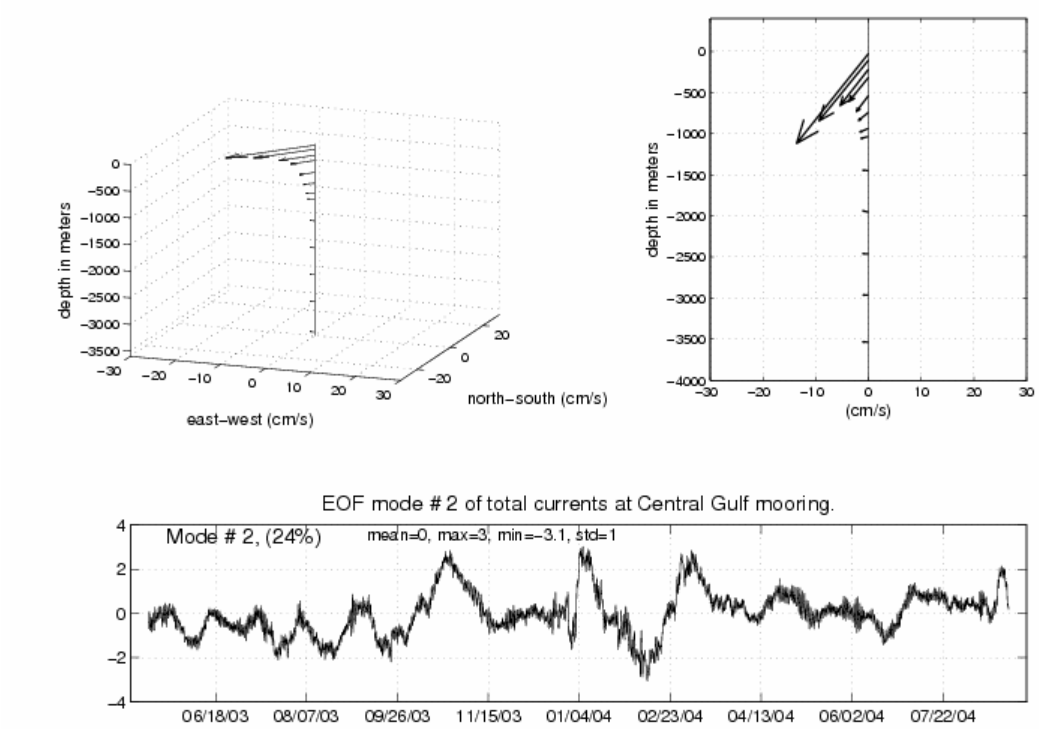

Figure 15b. As Figure 15a but for Mode 2 of the total observed currents.

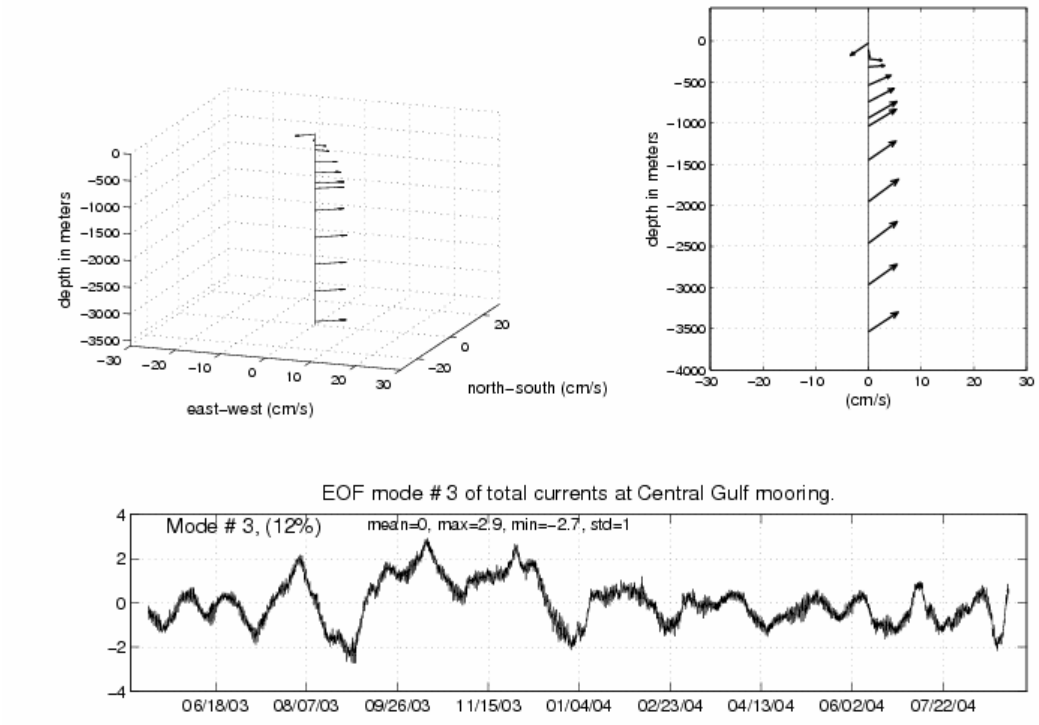

Figure 15c. As Figure 15a but for Mode 3 of the total observed currents.

From the principal components of the modes in Figure 15, it is clear that the supra-inertial content of the currents is small with respect to the sub-inertial variability. Using a low-pass Lanczos filter, with a 48 hour cut-off period, tidal and inertial oscillations are eliminated from the current time series as mentioned before. Although, as shown in Table 5, the sub-inertial variability dominates throughout the water column, it is interesting to see a relatively higher supra-inertial variability between 200 and 1000 meters depths, which is probably related to high internal wave activity at these depths.

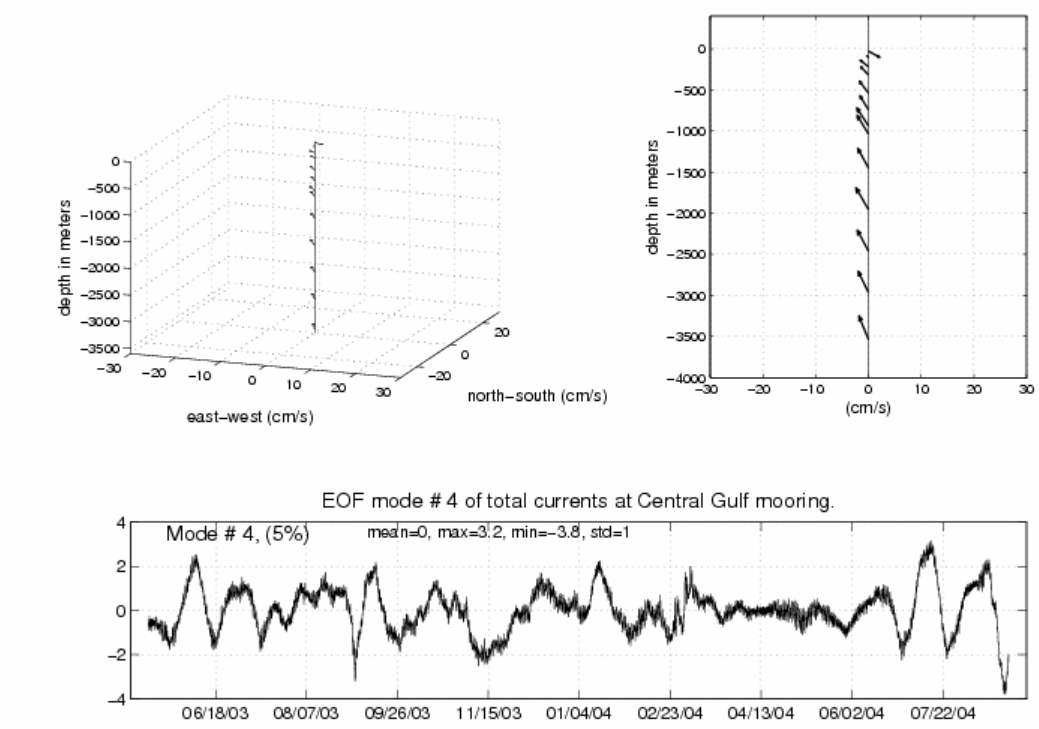

Figure 15d. As Figure 15a but for Mode 4 of the total observed currents.

Recall however, that this calculation is biased towards the surface (the region of highest variability) and is based purely on statistical orthogonality, which may explain the difference in energy partition between the EOFs and the dynamical modes. Since the sub-inertial bands dominate the observed variability 3 other EOF analyses were performed. Figure 16 shows the first 4 modes of the EOF decomposition of the subinertial observed currents, which, as expected, gives a very similar structure as the one obtained using the total currents. To diminish the effect of having arbitrary sampling levels that could certainly bias the variance distribution and modal structures, another EOF analysis was performed with series of currents interpolated every 10 meters along the water column.

Bear in mind though, that this interpolation does not eliminate the surface bias mentioned before. The first four modes of this analysis are shown in Figure 17. The vertical interpolation smoothly redistributes variance in the vertical. The results of this are that now the 4 modes have a more mixed barotropic and baroclinic structure.

To avoid biasing the calculation towards the surface, an additional EOF analysis was performed using the normalized (current components divided by their standard deviation) interpolated currents. The results are shown in Figure 18. By normalizing the currents one is basically obtaining the EOFs from the correlation matrix rather than the covariance matrix, and avoids giving too much weight to regions with large currents (like the surface in the present case) extracts the coherent structures without the magnitude weight. As seen in Figure 18, this approach yields patterns that tend to separate more clearly the barotropic (first two modes) and first baroclinic (modes 3 and 4) modes. It clearly eliminates the surface bias and in fact the modal structure of the first two EOFs (Figures 18a, b) has lower amplitude at the surface. Table 6 summarizes the percent of variability contained in the first four modes of all the EOF calculations discussed above.

The previous analysis shows that care should be exercised when interpreting EOF calculations. Both, the dynamical and statistical decompositions, are tools that provide information which can be used to interpret the observations, and should be carried out together as much as possible.

Table 6

Percentage of Explained Variance by the Four EOF Calculations

	Total % of Var.	Lowpass % of Var.	Interpolated Lowpass % of Var.	Normalized Lowpass %
Mode 1	49	53	35	56
Mode 2	24	25	31	25
Mode 3	12	12	17	10
Mode 4	5	5	13	5
Sum of modes 1 to 4	90	95	96	96

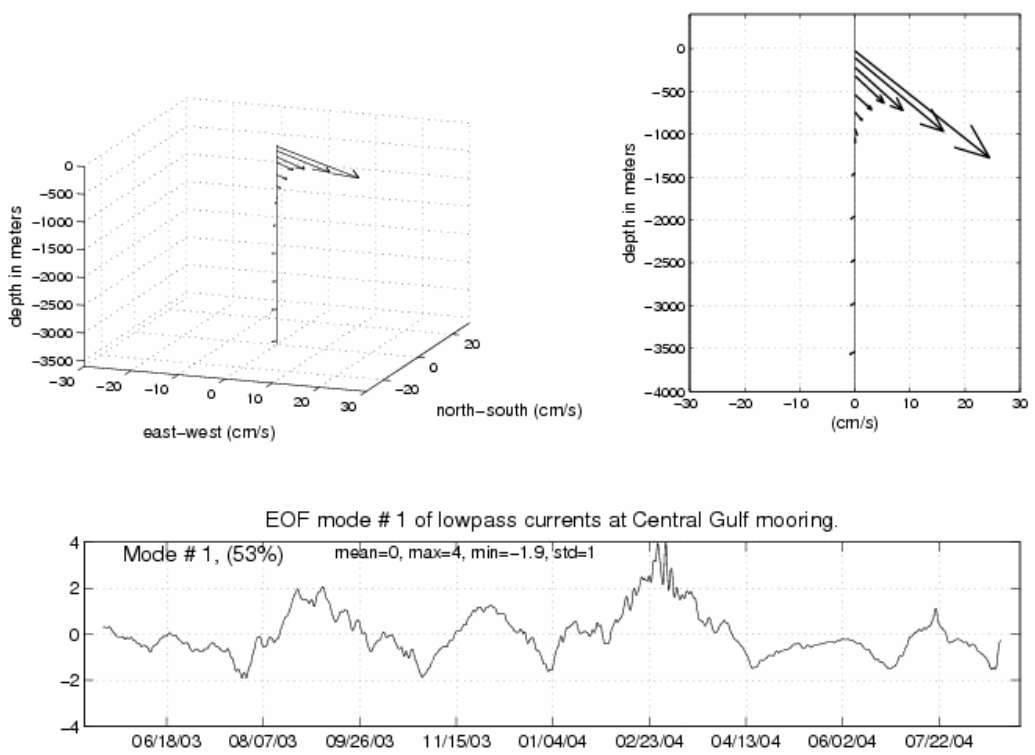

Figure 16a. As Figure 15a but for Mode 1 of the lowpass observed currents.

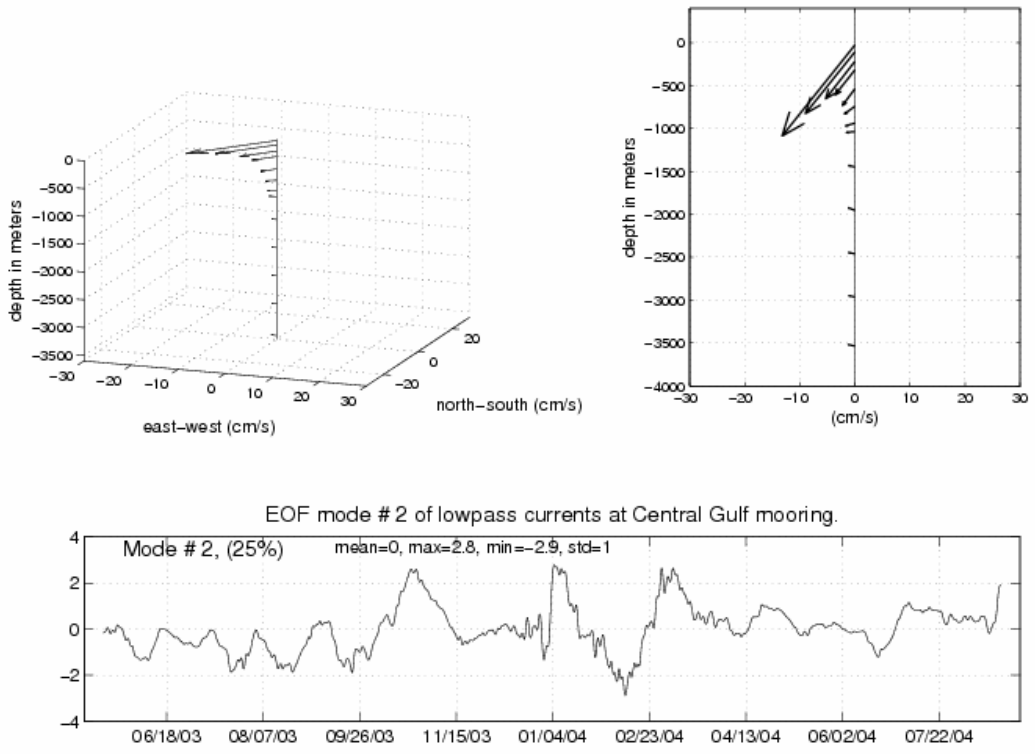

Figure 16b. As Figure 15a but for Mode 2 of the lowpass observed currents.

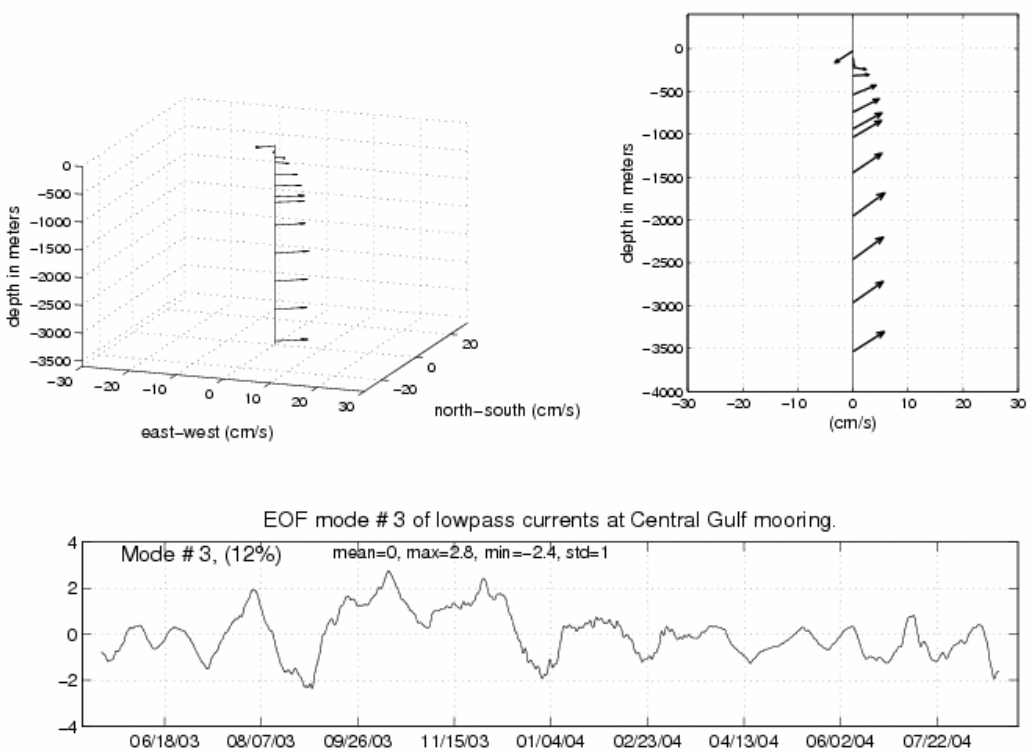

Figure 16c. As Figure 15a but for Mode 3 of the lowpass observed currents.

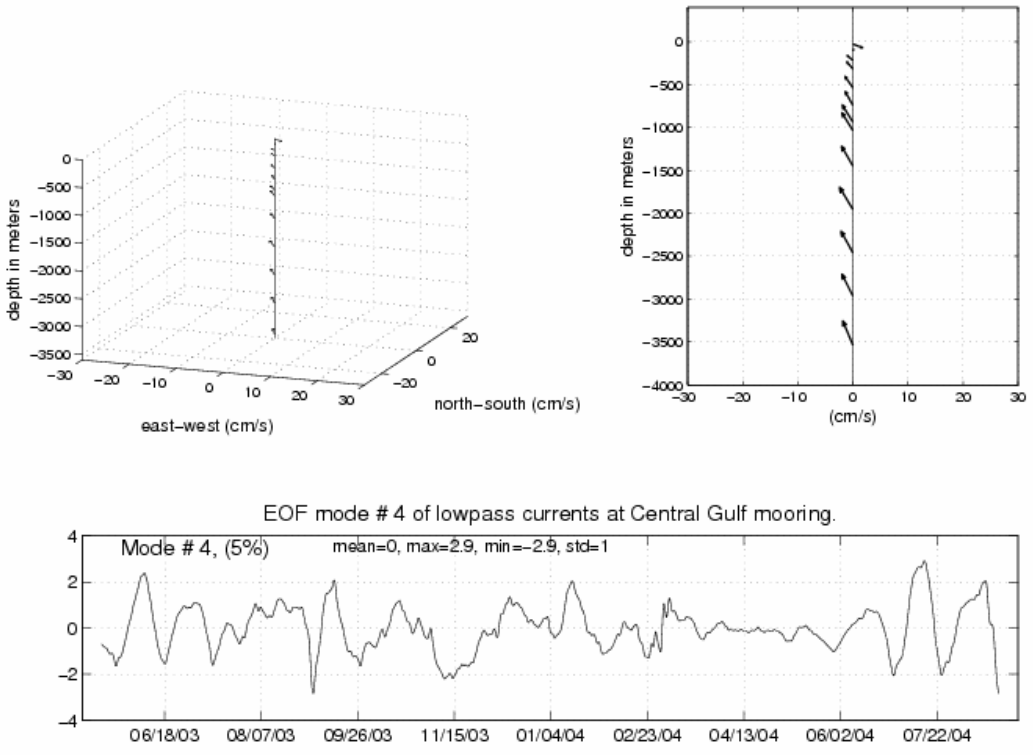

Figure 16d. As Figure 15a but for Mode 4 of the lowpass observed currents.

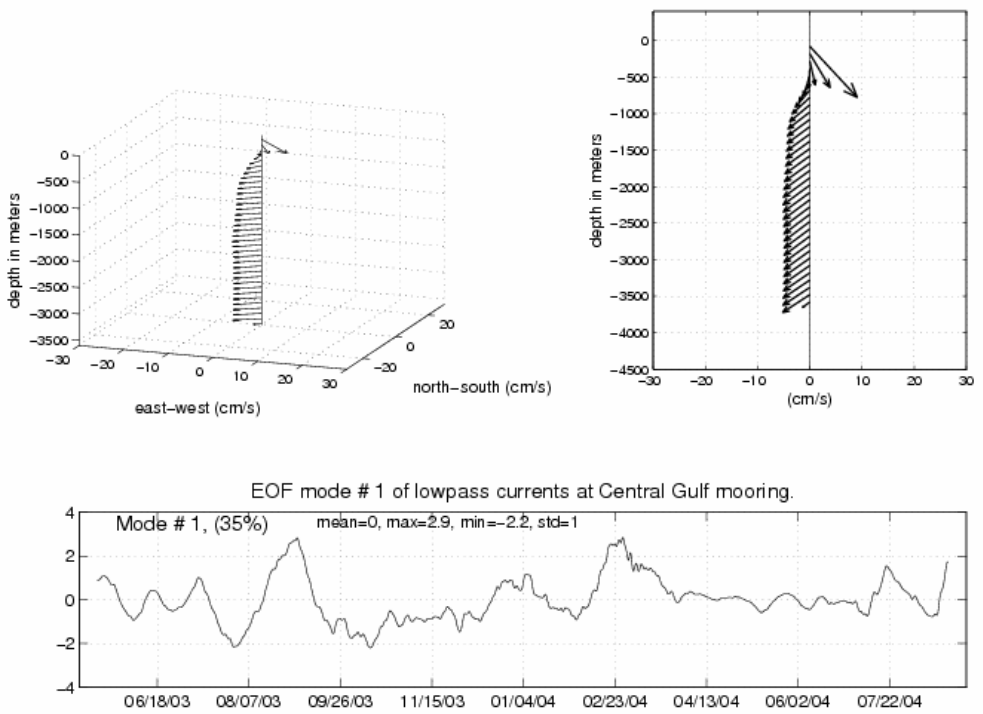

Figure 17a. As Figure 15a but for Mode 1 of the lowpass interpolated currents (Δz=10 m). Vectors in the upper 2 panels are plotted every 100 meters.

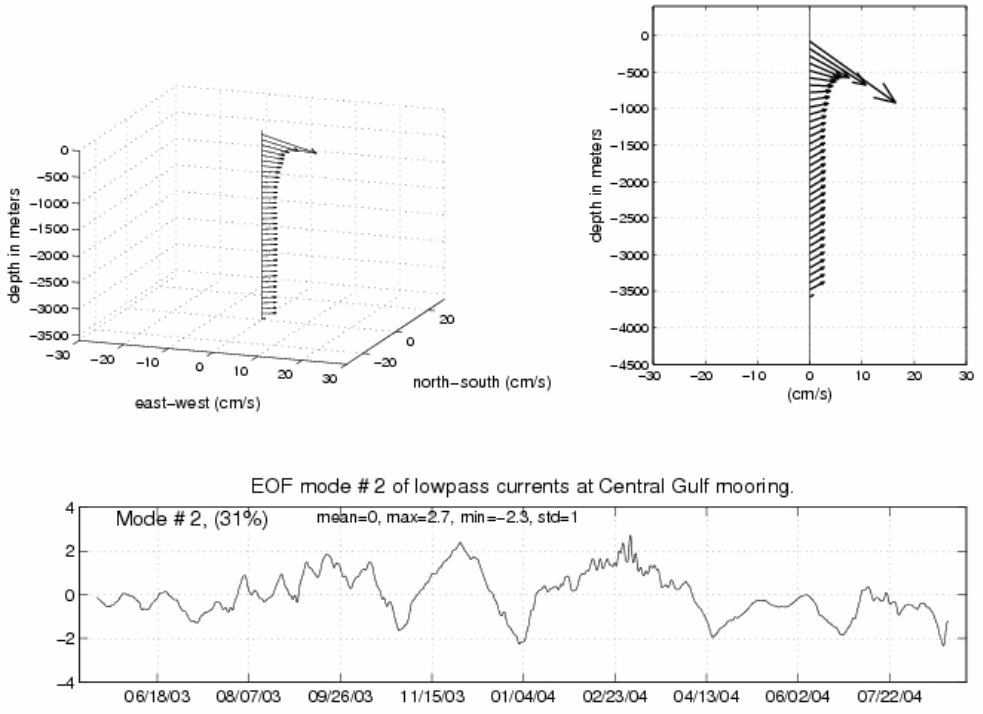

Figure 17b. As Figure 15a but for Mode 2 of the lowpass interpolated currents (Δz=10 m). Vectors in the upper 2 panels are plotted every 100 meters.

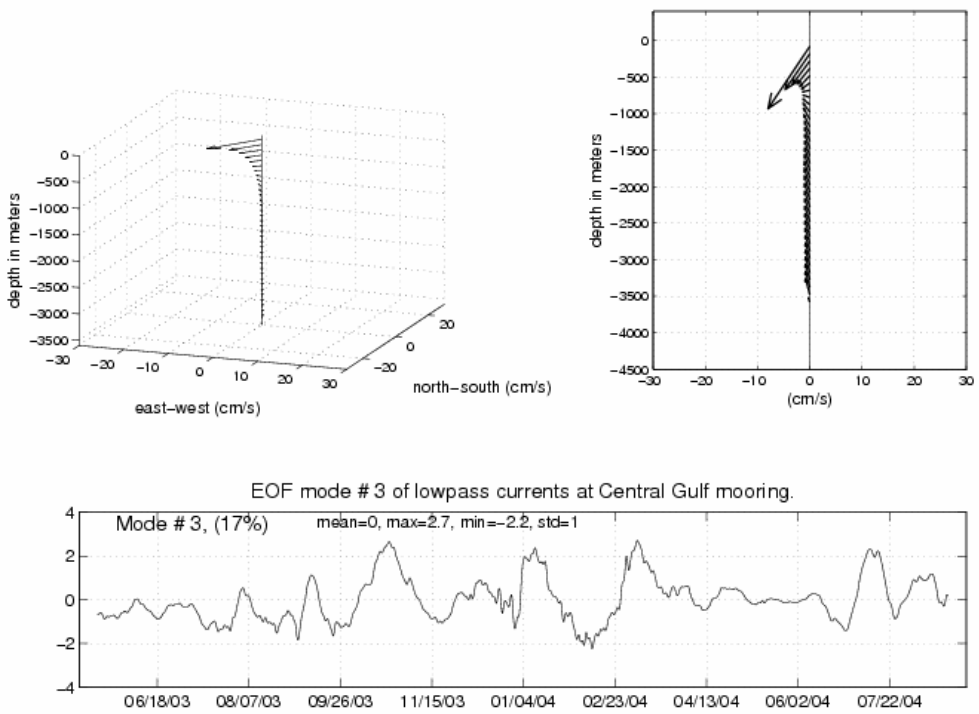

Figure 17c. As Figure 15a but for Mode 3 of the lowpass interpolated currents (Δz=10 m). Vectors in the upper 2 panels are plotted every 100 meters.

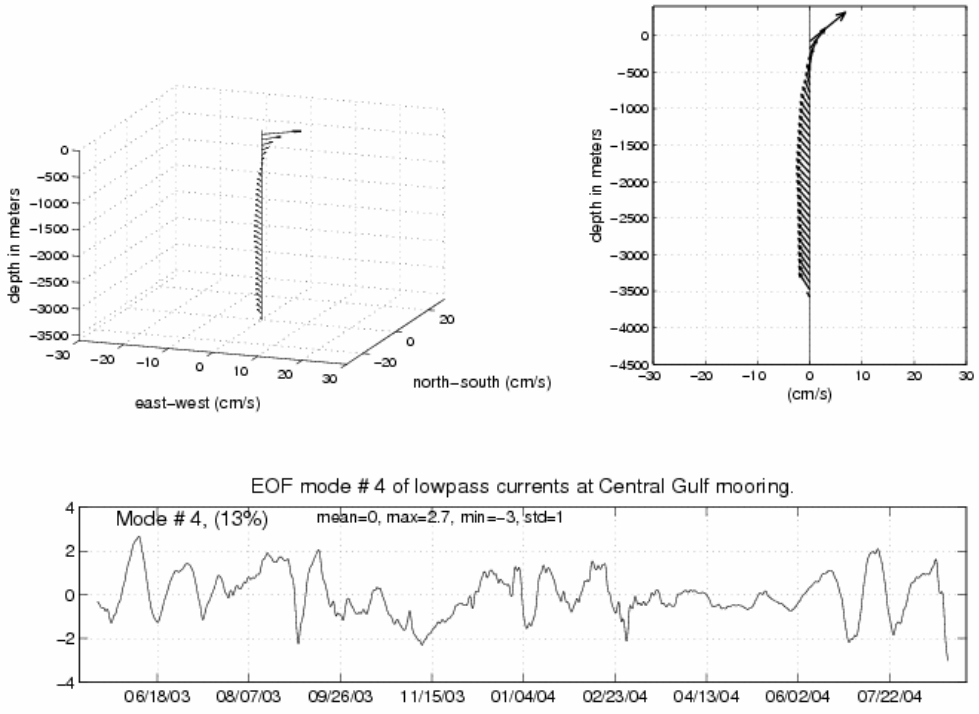

Figure 17d. As Figure 15a but for Mode 4 of the lowpass interpolated currents (Δz=10 m). Vectors in the upper 2 panels are plotted every 100 meters.

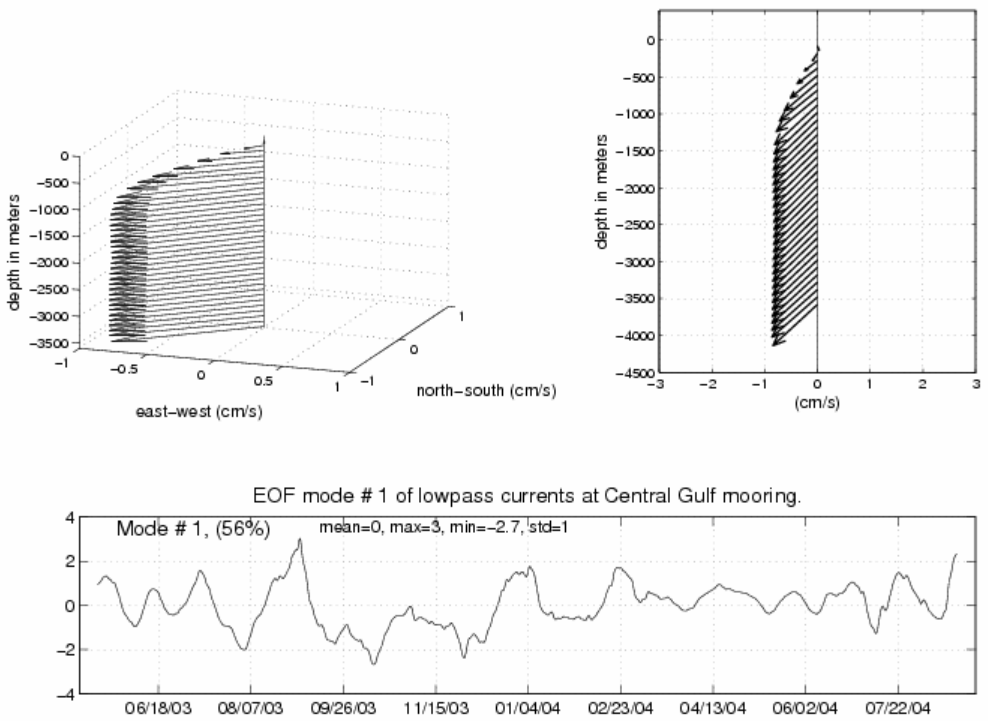

Figure 18a. As Figure 15a but for Mode 1 of the lowpass interpolated currents (Δz=10 m) normalized by the rms at each depth. Vectors in the upper 2 panels are plotted every 100 m.

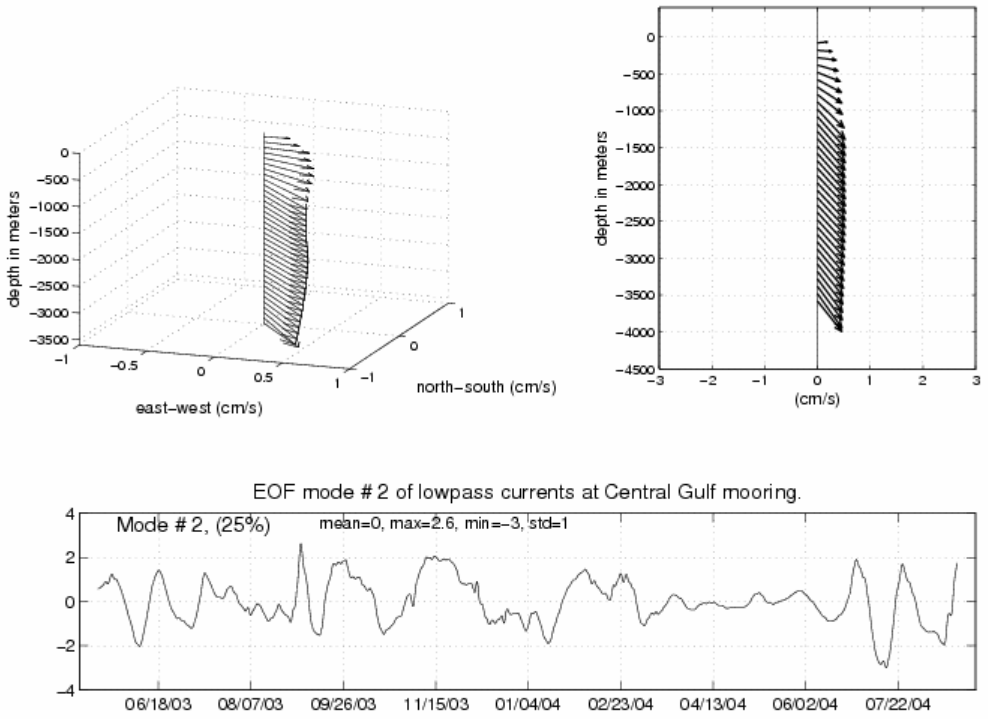

Figure 18b. As Figure 15a but for Mode 2 of the lowpass interpolated currents (Δz=10 m) normalized by the rms at each depth. Vectors in the upper 2 panels are plotted every 100 m.

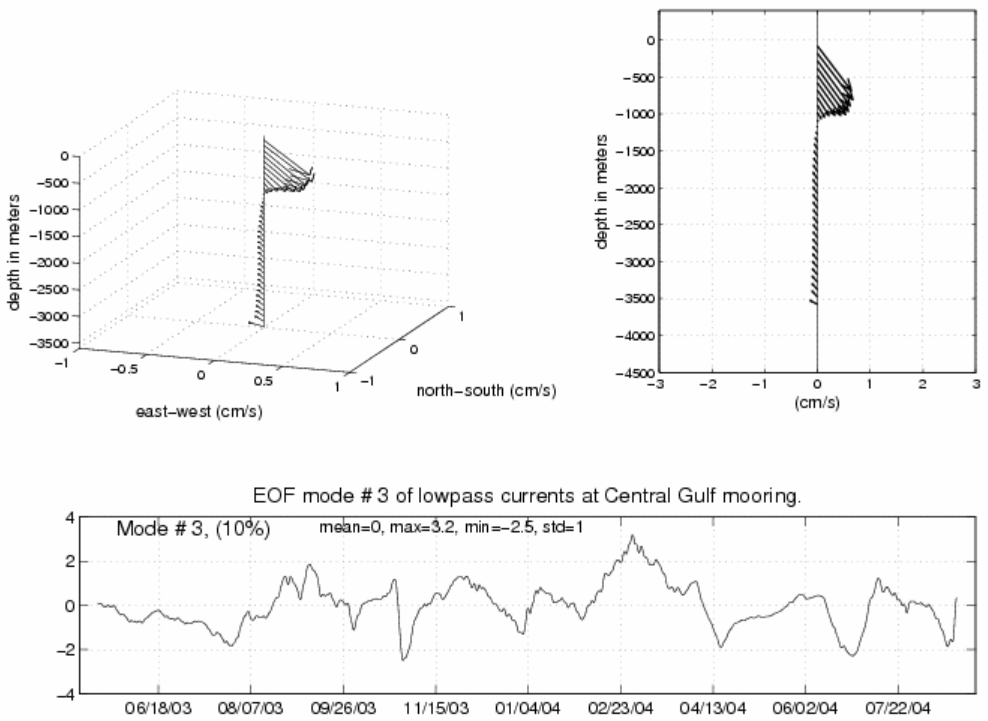

Figure 18c. As Figure 15a but for Mode 3 of the lowpass interpolated currents (Δz=10 m) normalized by the rms at each depth. Vectors in the upper 2 panels are plotted every 100 m.

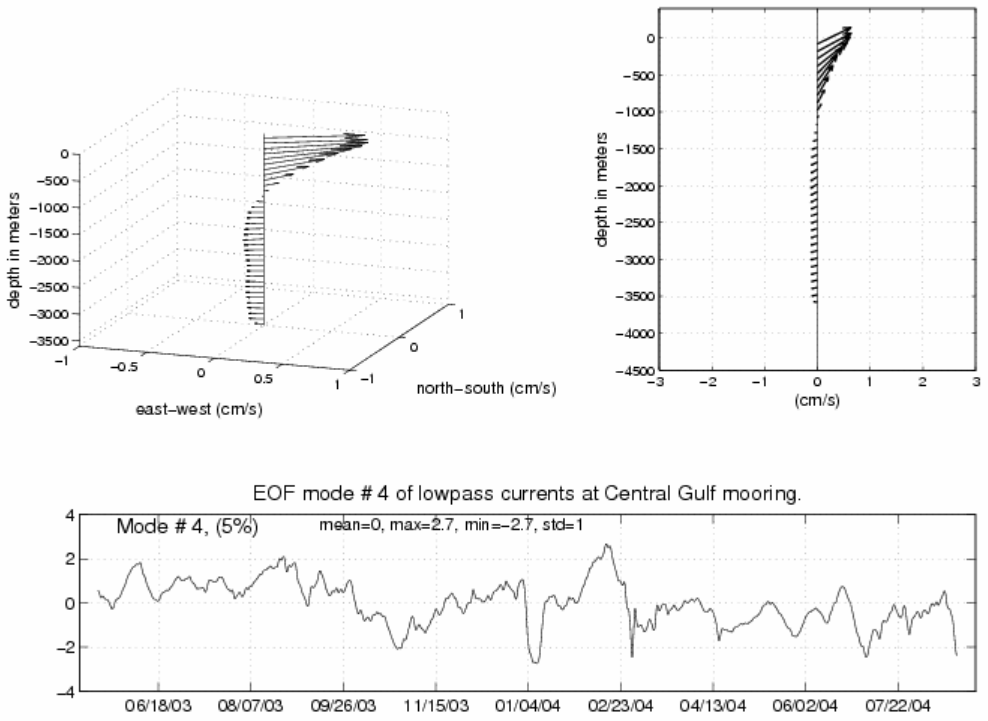

Figure 18d. As Figure 15a but for Mode 4 of the lowpass interpolated currents (Δz=10 m) normalized by the rms at each depth. Vectors in the upper 2 panels are plotted every 100 m.

4. Mooring Motion Corrections on Temperature Measurements: A Simple Method Based on Lagrangian Displacements and Dynamical Modes

A well-known problem with moored measurements is caused by the vertical displacements of the instruments, thus not measuring at the same position as needed in an Eulerian description of fluids. This is particularly important for computing temperature profiles, since low-pass currents are usually less sensitive to vertical displacements, when they are relatively small. The vertical displacements of moored instruments are known from the pressure sensors observations. Linear interpolation is usually carried out to obtain currents at nominal depths. However, the sensitivity of temperature to vertical displacements makes the temperature problem more difficult. It is therefore necessary to 'correct' for the variable vertical position of the measurements and infer what the temperature should be at a fixed vertical level based on previously obtained CTD casts or a climatology. Such data provides information of the mean vertical gradient of temperature as a function of temperature, so that a proper linear interpolation can be carried out (Hogg, 1991; Johns et al., 1995). Here we propose and perform a new method to compute mooring temperature profiles based on adiabatic vertical displacements of a reference profile or climatology, which provides similar results to the Johns et al. (1995) technique. We also complement this interpolation method using information from the dynamical modes. Simple by-products of this estimate are the time series of temperature at any fixed vertical position, in particular at the nominal instrument positions.

All the methods developed to estimate temperature time series at nominal depths available in the literature (such as Hogg, 1991; Johns et al., 1995) including the one proposed here, are based on the same assumption: the existence of an equilibrium (reference) temperature distribution. Variations of temperature in the vertical at any given time are due to adiabatic displacements/distortions of such reference profile. The method assumes the equilibrium profile is monotonic without mixed homogeneous layers and uses potential temperature (or, equivalently, the equilibrium depth of such potential temperature) as a Lagrangian label. From here on, unless otherwise noted, we simply use temperature as meaning potential temperature. In our case, CTD measurements, independent of the moored observations, determine the equilibrium profile. Then, each pair of depth (pressure) and temperature (one pair for each instrument) measurements is thus the result of a vertical displacement of the observed equilibrium temperature profile. For example, if potential temperature is 5 degrees at a depth of 1000 m, and one of the instruments measures 5 degrees at 900 m, one interprets such a measurement as a vertical displacement of 100 m of the 5 degree isotherm in the reference profile. Once the set of vertical displacements (one per instrument) distributed non-uniformly over the water column and in time is computed we can infer the continuous vertical displacement profile from surface to bottom. This last step requires, as in all known methods, an interpolation/extrapolation algorithm. The one we here implement is based either on a linear or polynomial interpolation or on a projection onto the internal dynamical modes that are directly computed from the equilibrium distributions.

4.1. Theory

Invoking adiabatic motion makes (potential) temperature, salinity, potential density and any other, so called, conservative variable a Lagrangian label, meaning that in an Eulerian

description, the field $\theta = \theta(\vec{r}, t)$ where θ is temperature or any other conservative variable, $\vec{r}$ is position and *t* is time, should fulfill

$$\theta(\vec{r} + \delta\vec{r}_{21}, t_2) = \theta(\vec{r}, t_1) \tag{2}$$

where $\delta\vec{r}_{21}$ is the displacement of (any and each) water parcel from t_1 to t_2. In other words, the water parcel keeps along, as it flows, the value of any conservative variable. This is a restatement or integral representation of the equation $D\theta / Dt = 0$, where the operator D / Dt is the material derivative; an equation that defines all Lagrangian conservative variables. Assuming the existence and knowledge of an 'equilibrium' *vertical profile* for temperature, Equation (2) states that observing a given temperature somewhere implies a specific vertical displacement: precisely the one required to observe that temperature away from its equilibrium level. In this context Equation (2) reads

$$\theta(\bar{z} + \varsigma(\bar{z}, t), t) = \Theta(\bar{z}), \tag{3}$$

where $\Theta = \Theta(\bar{z})$ is the equilibrium temperature distribution, which depends only on the vertical coordinate $\bar{z}$, and $\varsigma = \varsigma(\bar{z}, t)$ is the vertical displacement needed to observe $\theta = \Theta$ at the level $z = \bar{z} + \varsigma$. Another way to express Equation (3) is $\theta(z, t) = \Theta(\bar{z} - \varsigma(\bar{z}, t))$. A monotonic function $\Theta = \Theta(\bar{z})$ without homogeneous mixed layers from surface to bottom, allows to compute its inverse $\bar{z} = \bar{z}(\Theta)$, in which case the inverse of Equation (3) can be computed and reads

$$z(\Theta, t) = \bar{z}(\Theta) + \varsigma(\Theta, t). \tag{4}$$

The assumption of an equilibrium distribution that only depends on the vertical (i.e. a horizontally uniform equilibrium distribution) inhibits any possible determination of horizontal displacements, but allows the unambiguous determination of vertical displacements. In Equation (3) the use of the symbol θ or Θ for the independent variable makes no difference. As discussed, among others, by Ripa (1981, 1990), one can invert the role of the independent and dependent variables. Thus, instead of describing the vertical profile with temperature as dependent and depth as the independent variable, (i.e. $\theta = \theta(z, t)$), the inverse of such expression (i.e. $z = z(\theta, t)$) is also valid and very useful for our purposes. Using potential temperature referred to the surface as our independent variable, the vertical displacement is computed out of Equation (4) by

$$\varsigma(\Theta, t) = \bar{z}(\Theta) - z(\Theta, t), \tag{5}$$

and the 'profile' $\varsigma = \varsigma(\Theta, t)$ is as valid as $\varsigma = \varsigma(\bar{z}, t)$ since $\Theta = \Theta(\bar{z})$ and its inverse $\bar{z} = \bar{z}(\Theta)$ are available, i.e. the choice of the Lagrangian label is up to the user. We use these theoretical results for mooring motion corrections.

4.2. Application to Correcting Mooring Motion

Figure 19 shows a reference potential temperature profile at nearby positions of the MMS-CICESE mooring estimated from 2 CTD profiles, one made prior to deployment and the other immediately after recovery. One obviously needs more profiles to estimate a sensible equilibrium profile, but searching for profiles in that position in the climatic and oceanic data bases, (e.g. NODC) on the web only one profile was found sufficiently close to the mooring position.

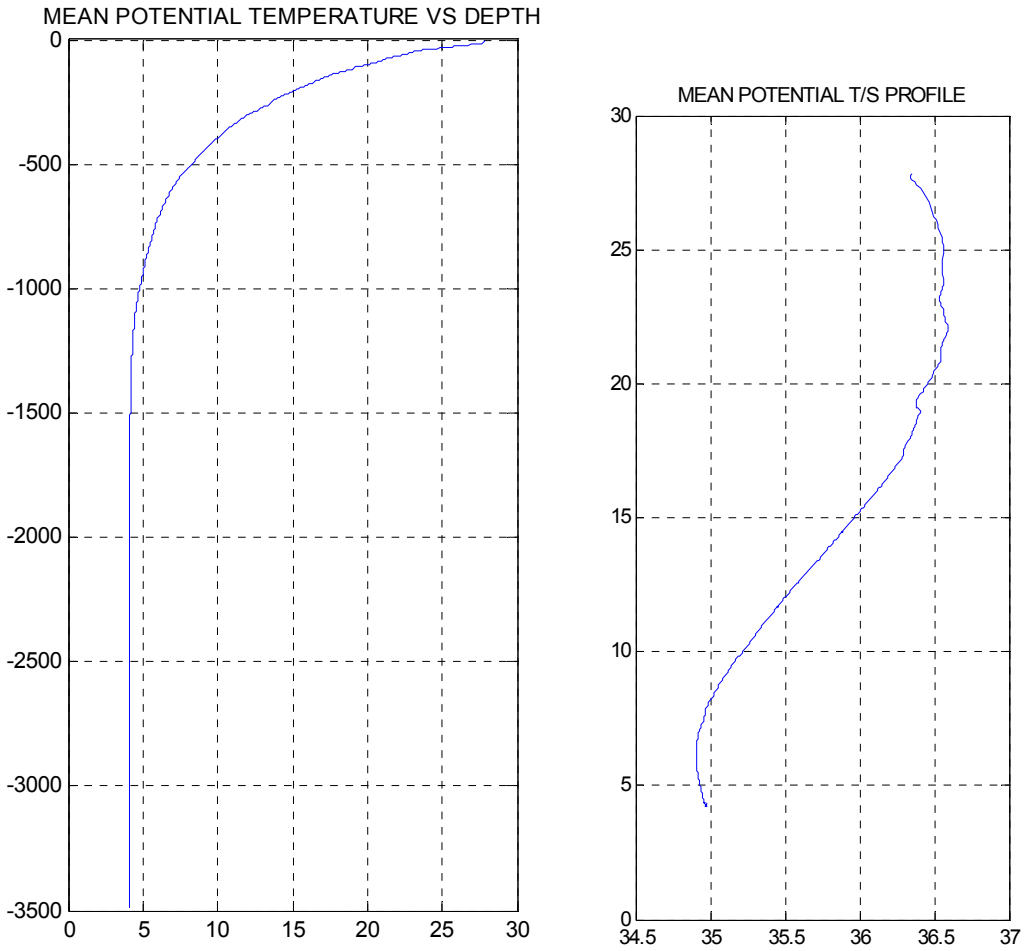

Figure 19. Potential temperature mean distribution in the Gulf of Mexico as a function of depth (left) and salinity (right).

To compute potential temperature an instantaneous salinity, assigned via the mean T/S diagram derived from CTD observations and shown in Figure 19, is used. This step is carried out for consistency with the adiabatic assumption and, given its crudeness, produces insignificant variations whether in situ temperature or potential temperature is used as Lagrangian label.

In the MMS-CICESE mooring the 3 ADCPs had pressure sensors. The whole mooring vertical motion was estimated by fitting a catenary function to the available pressure measurements. Once the moored instruments, either the Aanderaa or ADCP, vertical positions are computed, the pair of depth and temperature time-series registered produce estimates of vertical displacements of water particles, although from differing equilibrium levels (Equation (4)).

Figure 20 shows the vertical displacements of the instruments (each shifted by 100 meters, going from surface to bottom) showing maxima of vertical movement of around 80 meters.

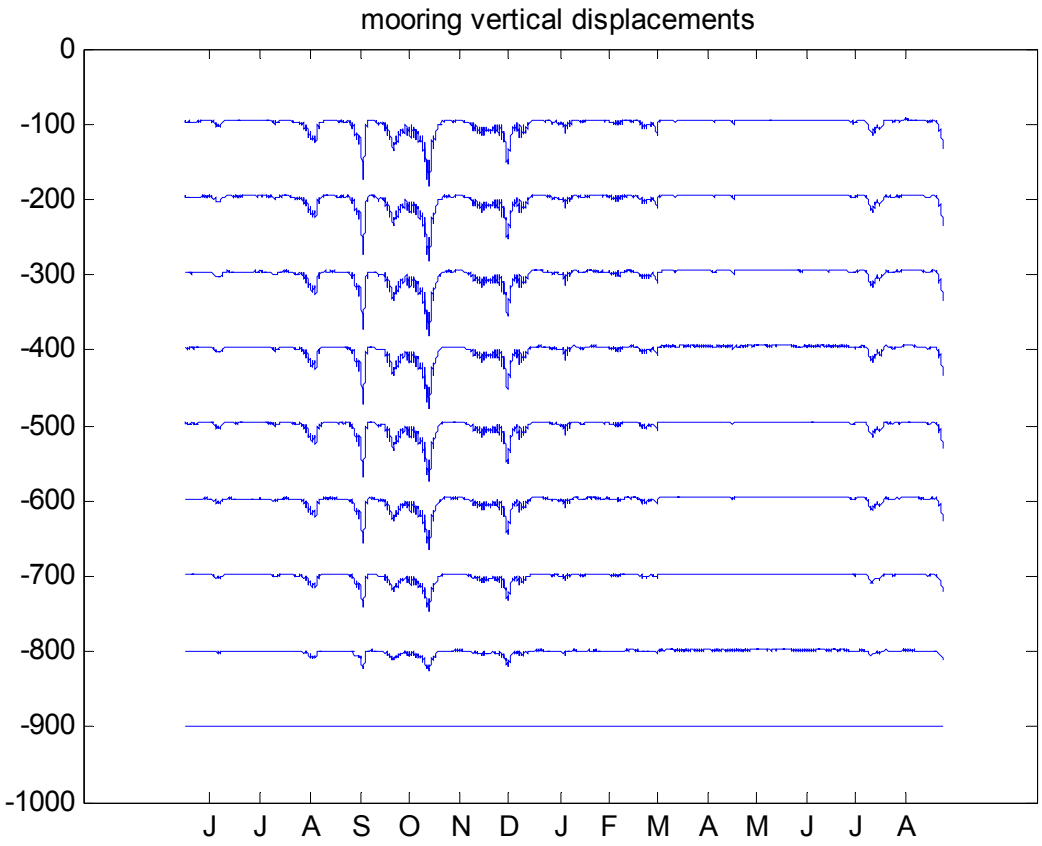

Figure 20. Mooring vertical displacements estimated based on a catenary profile for the mooring cable and pressure data from the ADCPs. Depths are shifted by 100 m from top to bottom for clarity.

To apply the mooring motion correction method to the potential temperature profiles, we first filter the potential temperature (PT) and depth (i.e. pressure) series using a Lanczos filter with a half power cut-off frequency of 1/48 hours^{-1}. We then estimate the vertical displacements using Equation (4). Since the instantaneous depth z and temperature θ are known from the measurements, we calculate $\bar{z} = \bar{z}(\theta)$. This determines the Lagrangian "label", in this case the vertical position that a particle with potential temperature θ has in the reference profile. Once the vertical displacements associated with a set of $\bar{z}_i$'s, are available, they can be interpolated to the nominal depths or any desirable depth. Lacking any other information, a linear interpolation

of the available $\varsigma_i \equiv \varsigma(\bar{z}_i, t), i = 1,..,6$ is carried out. Figure 21 shows an example of this procedure in which the available ς_i are interpolated to the whole water column. The interpolation is performed assuming zero vertical displacements at the bottom and at the surface and interpolating just the top 6 "measured" ς_i, since the ones below imply very large displacements whose impact on the estimated temperature is very small, due to the nearly well mixed character of the deep ocean, and may not be very realistic.

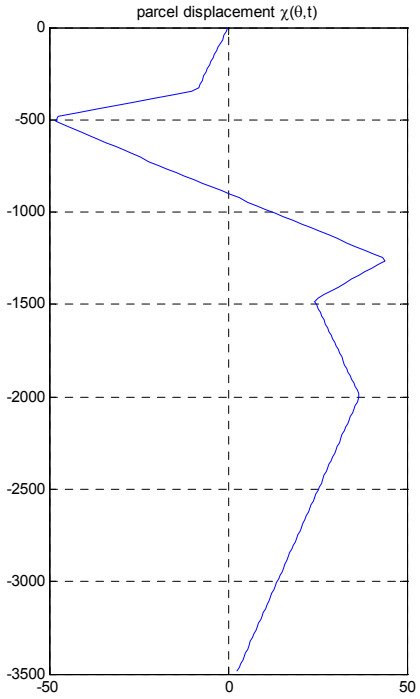

Figure 21. Realization of the vertical excursion interpolation.

Once the vertical displacements at all depths are estimated, a continuous temperature profile can be estimated using Equation (4). Figure 22 shows the low-passed temperature profiles estimated using this procedure:

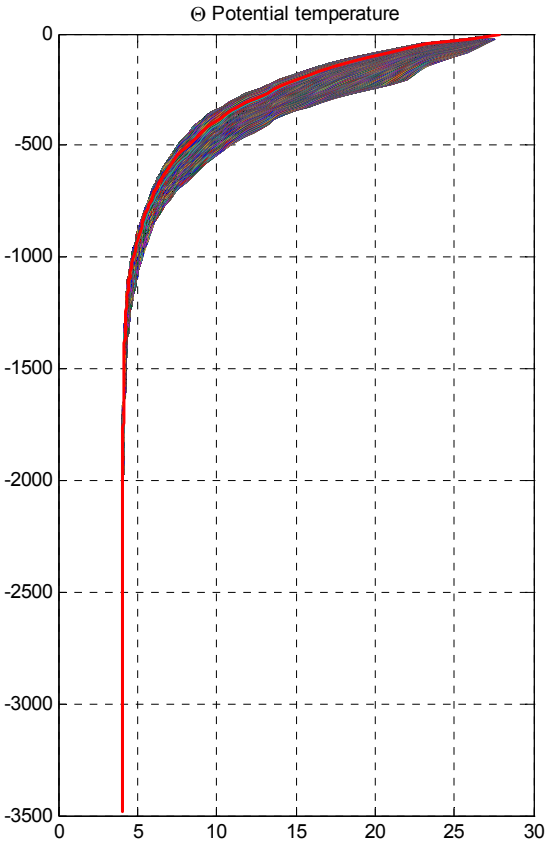

Figure 22. Reconstructed potential temperature profiles using linear interpolation. The thick red line represents the reference profile.

The thick line represents the reference temperature profile. The method will work well at nominal depths but linear interpolation of displacements is not a good approximation over large depth separations. To add more structure based on dynamics to this estimate, the vertical displacements (see Figure 21) are projected on the dynamical normal modes which solely depend on the equilibrium stratification. As example of this projection, a realization is shown in Figure 23. Recall that these modes, orthogonal using $N^2 = N^2(z)$ as weighting function, form a complete basis; the linearly interpolated profile (or any other) is reproduced exactly using the full set of modes. Although using the first 11 modes (green line in Figure 23) always reproduces better the linearly interpolated profile (red line in Figure 23) than with the first 4 modes (black line in Figure 23), only the first 4 mode are used for the reconstruction, since as discussed in Section 2, these 4 modes represent most of the velocity variance. Figure 24 shows the $\theta(z,t) = \Theta(\bar{z} - \varsigma(\bar{z},t))$ profiles using only 4 dynamical modes to estimate the continuous vertical displacement field. N^2 must be smooth so irregular "wiggles" are not reproduced in the displacement profiles. Once the profiles are calculated other calculations such as eddy heat fluxes, etc can be carried out.

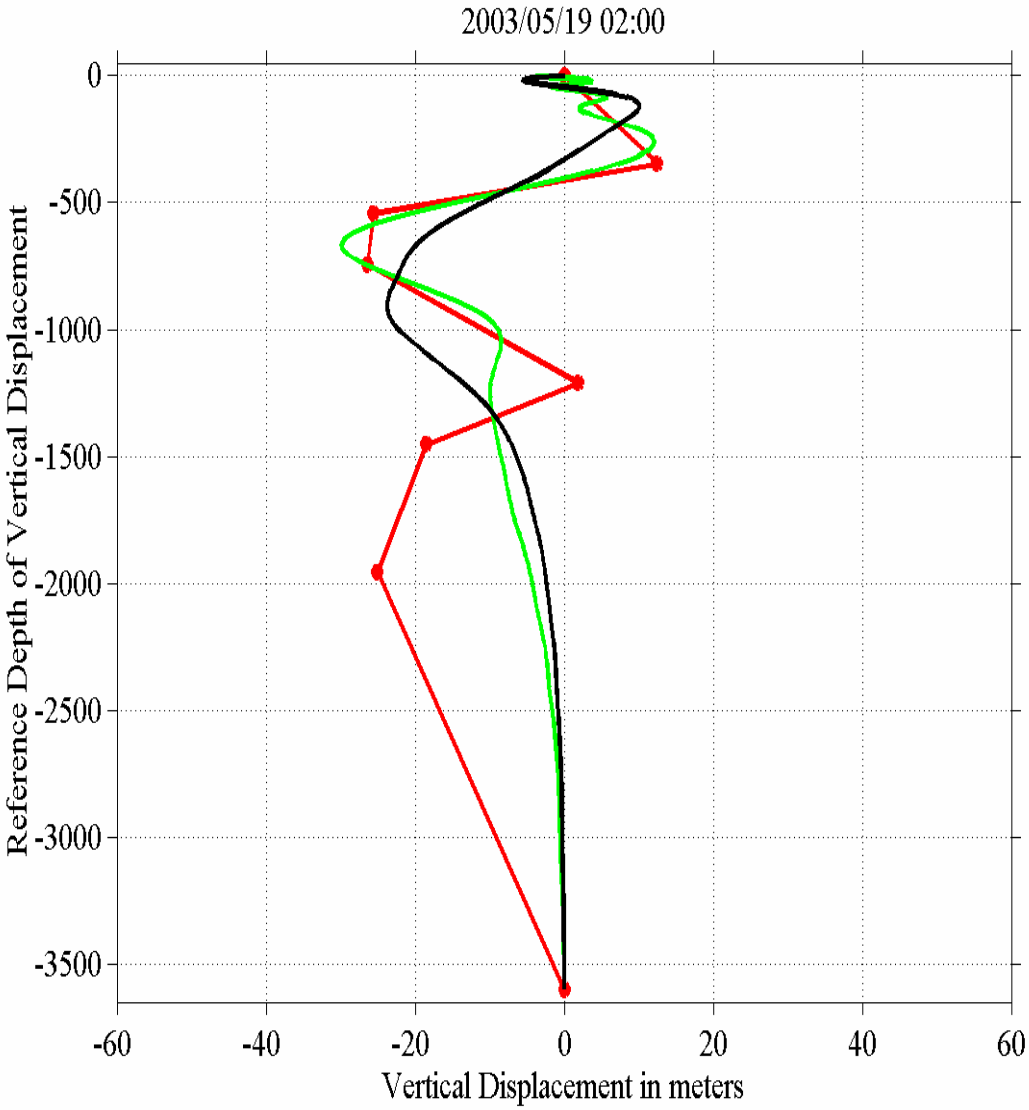

Figure 23. Reconstruction of a vertical displacement profile (linear interpolation, in red) using projection on dynamical normal modes. The reconstruction with the first 4 modes is in black, with 11 modes in green.

The method appears to work reasonably well (or as well as other methods available) and can produce smooth vertical temperature profiles or estimates of temperature at specified depths, which are consistent with the observations, the assumption of potential temperature conservation (Equations 3 and 4), and the reference or climatological profile.

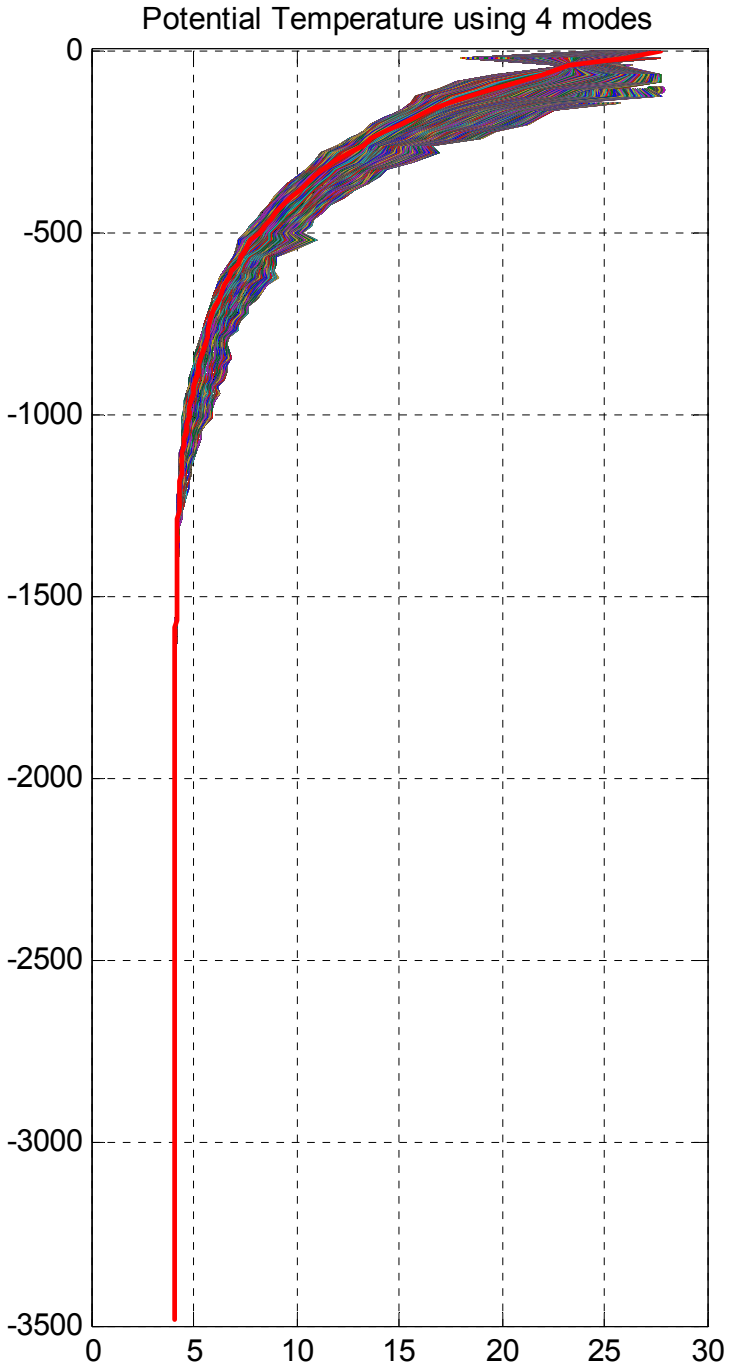

Figure 24. Reconstruction of potential temperature profiles using 4 dynamical modes.

5. Eddies and Their Relation to the Observed Variability

The low frequency velocity fluctuations shown in the vector time series of Figure 9 are clearly related to the passage of eddies close or nearly above the mooring as is shown next. Figure 25 shows snap-shots of sea surface height anomalies (ssha) obtained from the AVISO analysis of TOPEX/ERS altimetry data. During our observation period, formation of four vortical structures from the Loop Current occurred. The first one was a "small" anticyclone which formed in the southeastern edge of a large anticyclone nearly detached from the Loop Current, east-southeast of the mooring location, and shed from it in early August 2003. This type of small anticylonic eddies are commonly shed from the Loop Current, as well as from the larger warm-core rings, through their interactions with peripheral cyclones (Schmitz 2005; Leben 2005).

As will be shown below, this minor eddy (hereafter referred to as MEd) had important effects in the observation series. The other eddy-formation events correspond to three of the so-called Loop Current Eddies, ``Sargassum", ``Titanic" and ``Ulysses" (hereafter referred to as SEd, TEd and UEd), as they were named by the Eddy Watch program held by Horizon Marine, Inc, (www.horizonmarine.com). SEd, the larger anticyclone from which MEd detached, was already formed at the beginning of our observation period; this showed periods of near separation and vigorous interaction with the Loop Current, up to its complete separation in early August 2003; this long and complicated process was also confirmed by ocean color imagery (Chassignet et al., 2005). However, TEd's separation took less time, since it shed from the Loop at the end December 2003, barely five months later than SEd's separation.

Subsequently, UEd's separation occurred on about mid September 2004, roughly two weeks after the ending of our observation period, hence this eddy did not impact our measurements. Interestingly, a typical feature in the shedding events is the development of a band of cyclonic vorticity (sea-level trough) between the eddy and the Loop Current, which appears to favor the separation process; this is consistent with scenarios discussed by Chérubin et al. (2005) and Schmitz (2005). After the shedding of UEd, the Loop Current developed an intense trough north the Yucatan Channel, a feature that lasted about two months.

The first event, which occurred on September 2003 (Figure 25), is associated with MEd passing over the mooring. Once shed from the Loop Current, MEd drifted westward and subsequently interacted with SEd. Figure 25 shows that SEd is located northeast of the mooring and drifting westward but it has no influence on our measurements as of September 2003.

After its separation from the Loop Current, SEd drifted westward roughly following the 1500 m isobath until it apparently ``felt" the presence of MEd and stopped drifting westward, it then started drifting southward towards MEd. After three weeks, SEd drifted southward and reached the mooring location, and its merging with MEd, apparently absorbing it. By mid-November, MEd has been completely destroyed, with a single eddy remaining, containing vorticity from the two original eddies. The merging lasted about one month and a half. Finally, once shed, TEd started drifting westward with intense cyclonic vorticity in its northern edge, appearing as a dipole. This structure reached the mooring at the end January 2004, and its passage lasted two

months. This eddy was clearly detected as intense, coherent signals in velocity and temperature in the mooring as shown below.

(a)

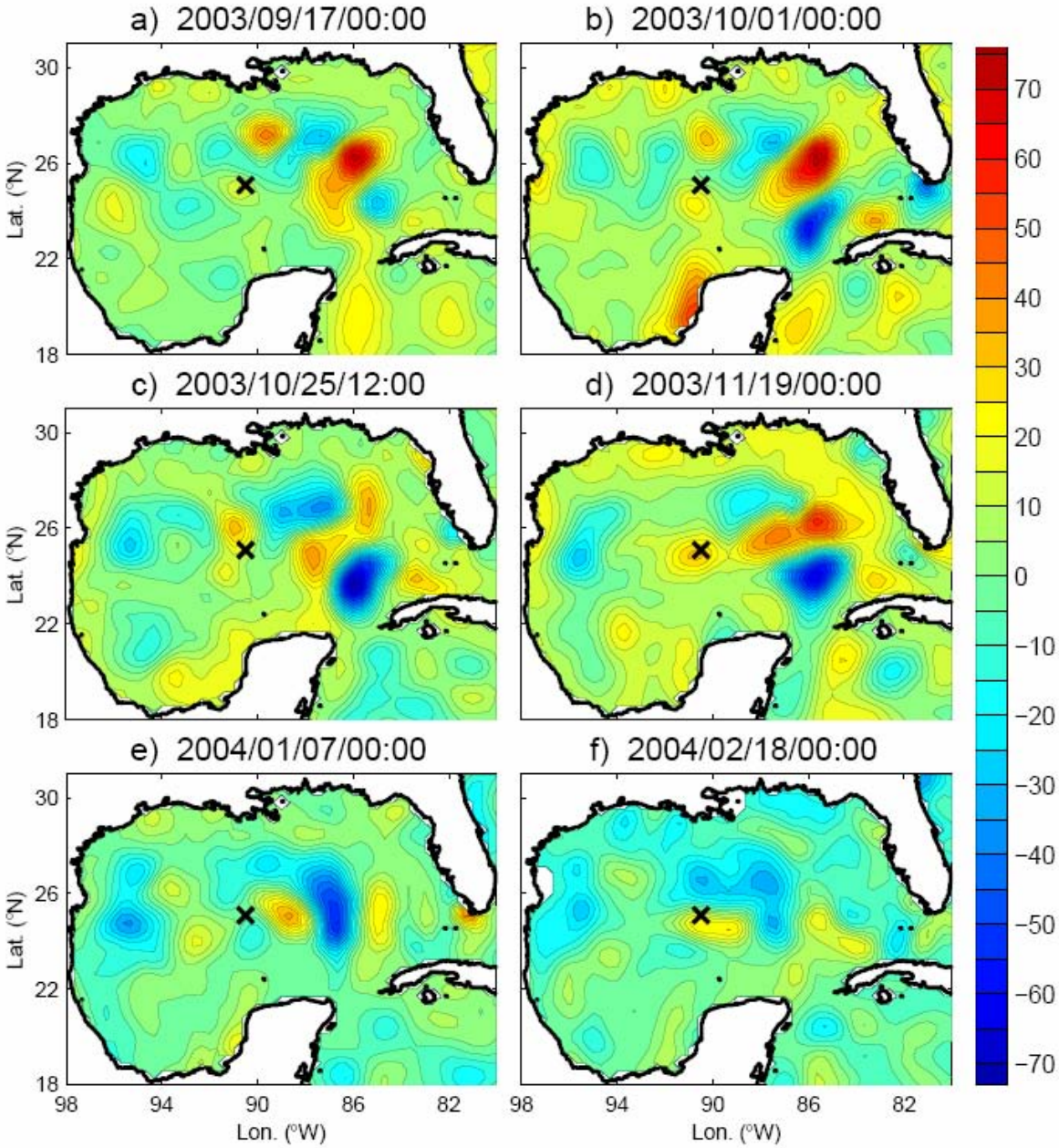

Figure 25a. Snap-shots of sea surface height anomalies obtained from the AVISO gridded analysis. Some of the depicted cyclones and anticyclones going over or close to the mooring were actually named by the Eddy Watch Program, (Horizon Marine Inc). The cross in all Figure 25 plots marks the position of the mooring and the white contours represent the Okubo-Weiss parameter.

(b)

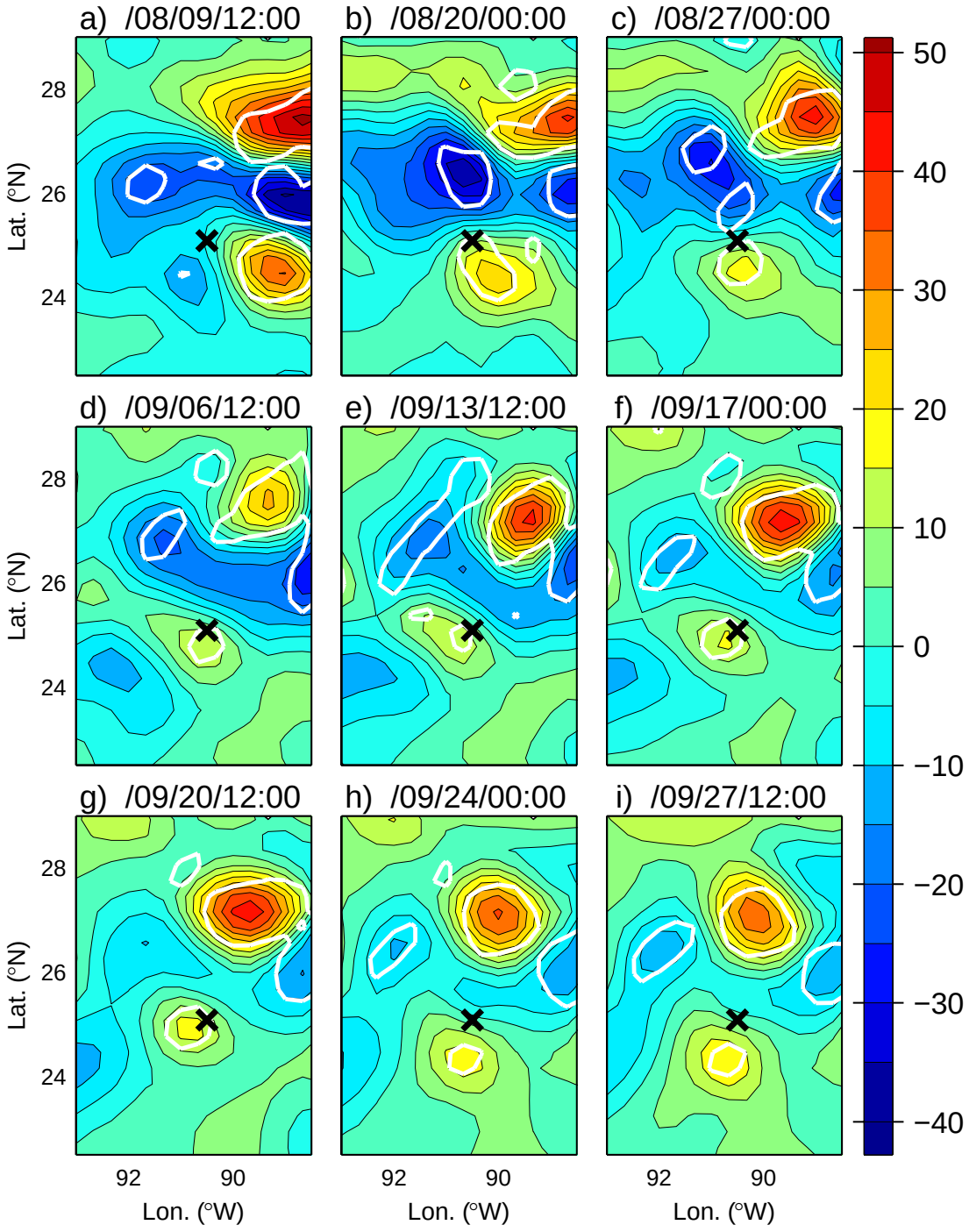

Figure 25b. Details of the time evolution of the MEd eddy from the ssha data.

(c)

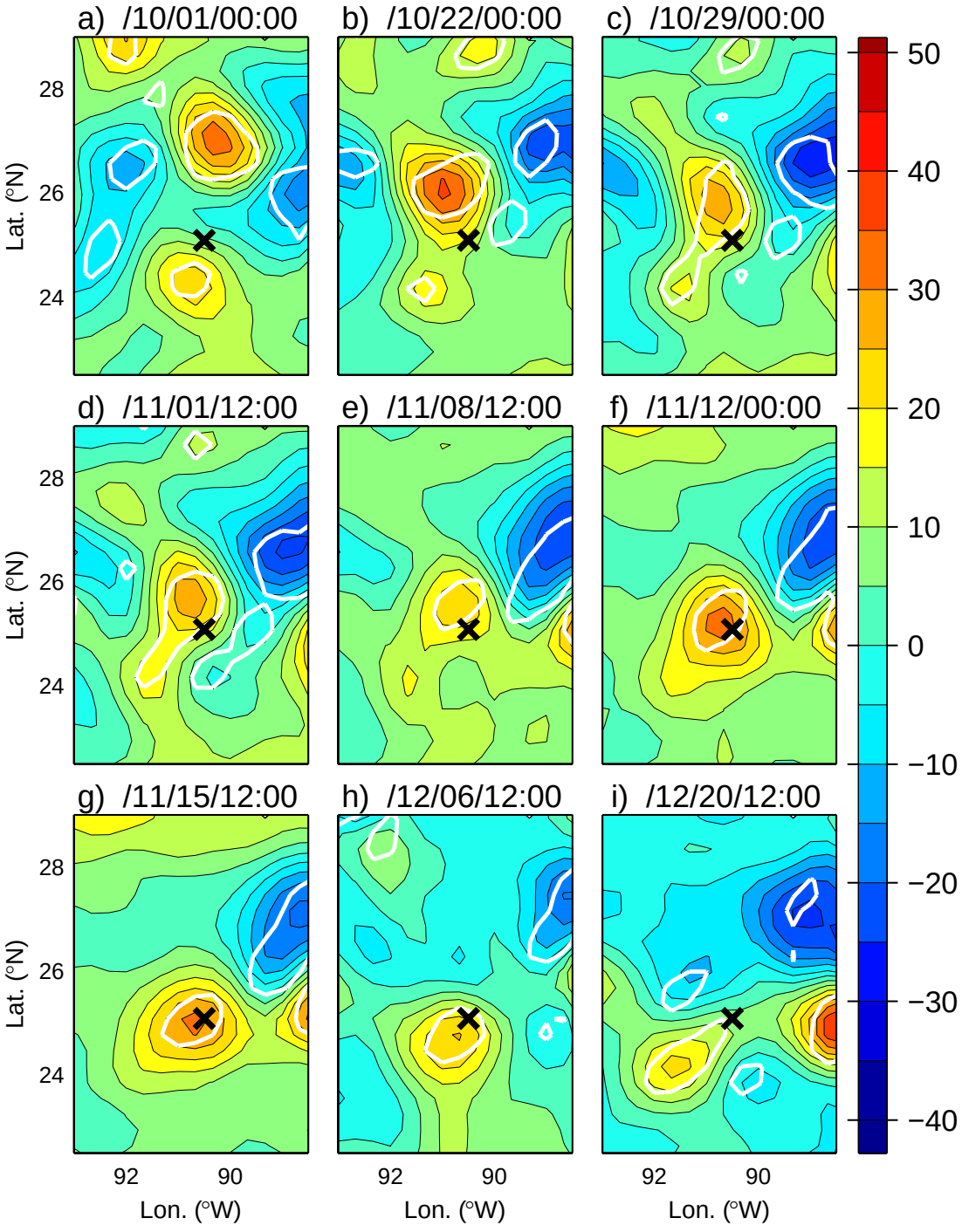

Figure 25c. Details of the time evolution of the SEd eddy.

(d)

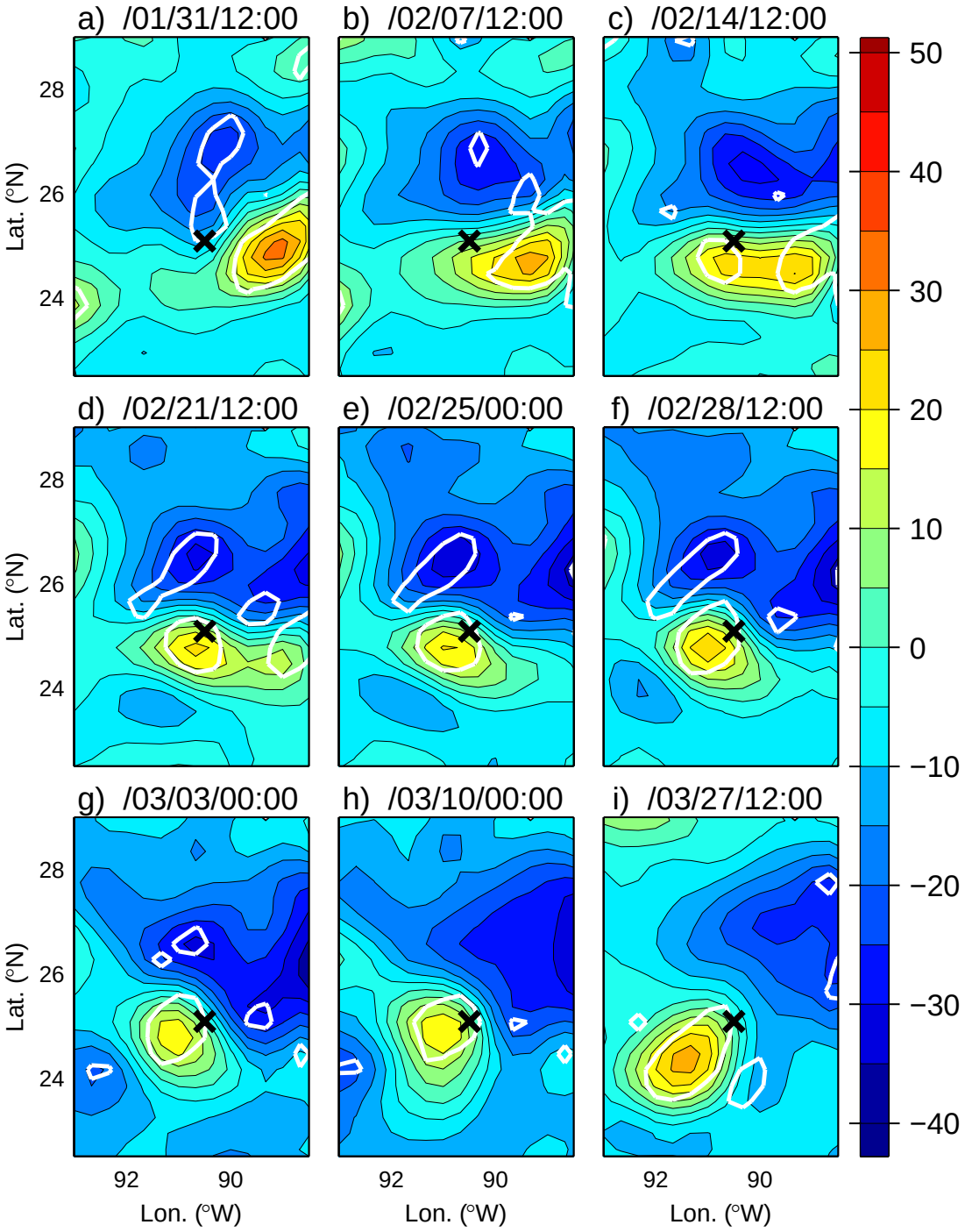

Figure 25d. Details of the time evolution of the TEd eddy.

Figure 26 shows vertical time-series of zonal, meridional and vertical low-pass velocity anomalies from the mooring data, as a function of depth during the deployment period. The vertical bars in the Figure 26 highlight the periods when the above mentioned eddies were nearby the mooring and correspond to the snap-shots shown in Figure 25.

Correspondence between the eddy events and the increase in absolute value of the velocity anomalies is striking. It is also worth noticing the vertical structure of the signal and its influence depth. Although largest anomalies are usually confined to the top 300 meters of the water column, the eddy signal can be detected down to 1200 m. Observe also that there are events, such as in November 2003, where the anomaly signal may be stronger at mid-depth (see panel b, Figure 26). We consider only horizontal velocity anomalies for the analysis. The possible use and interpretation of vertical velocities is discussed in Rivas et al. (2006, submitted).

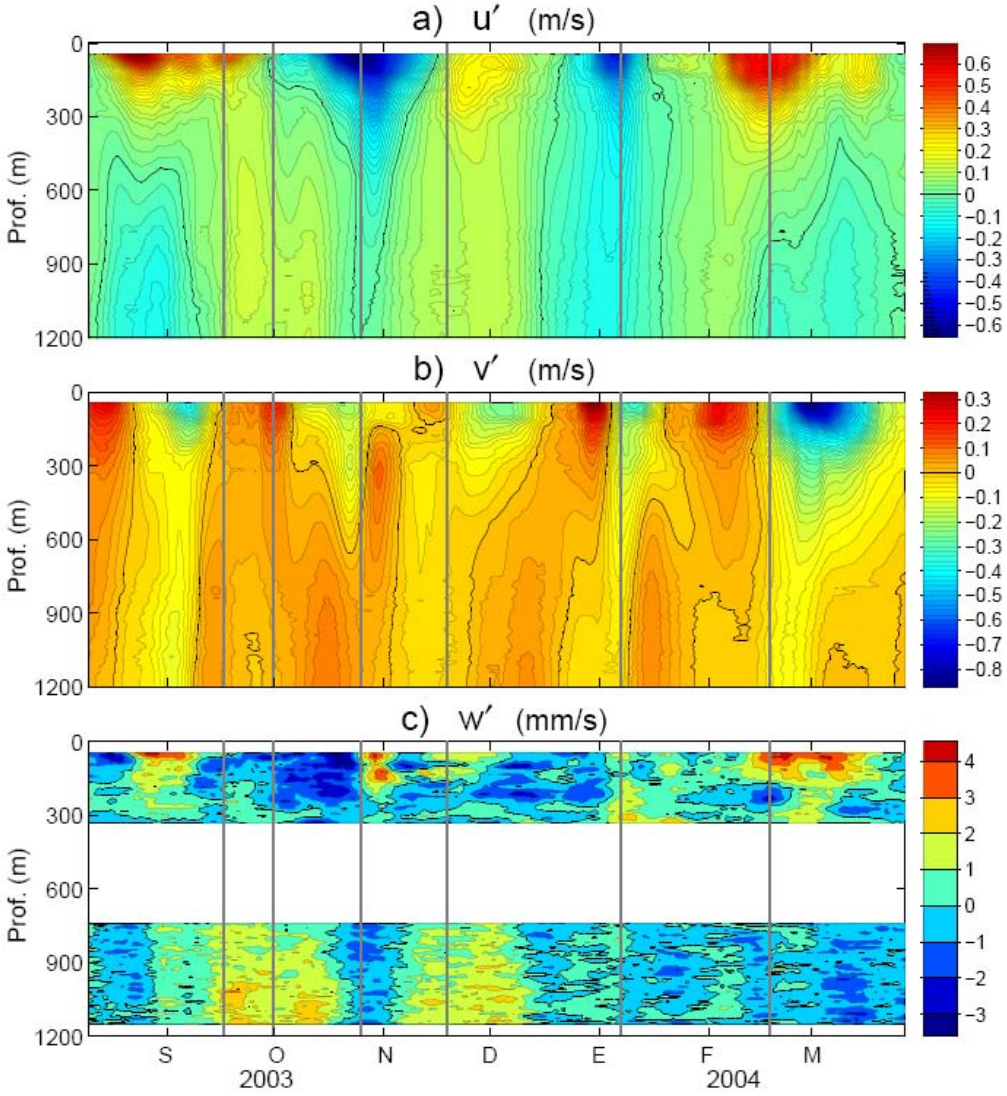

Figure 26. Zonal, meridional, and vertical low-pass velocity anomalies from the mooring data, as a function of depth and time. The vertical bars in the Figure highlight the periods when eddies were nearby the mooring and correspond to the snap-shots shown in Figure 25.

Figure 27 shows stickplot diagrams together with vertical displacements of the isotherms at the corresponding depths. It is interesting to compare these figures with the eddy events identified by altimetry data in which three eddies came close or cross over the mooring (see Figures 25 and 26). The passage of anticyclones or cyclones do coincide with a deepening and shallowing of isotherms respectively and, as Figure 28 shows, isothermal vertical displacements are quite coherent in the water column down to 1500 m.

(a)

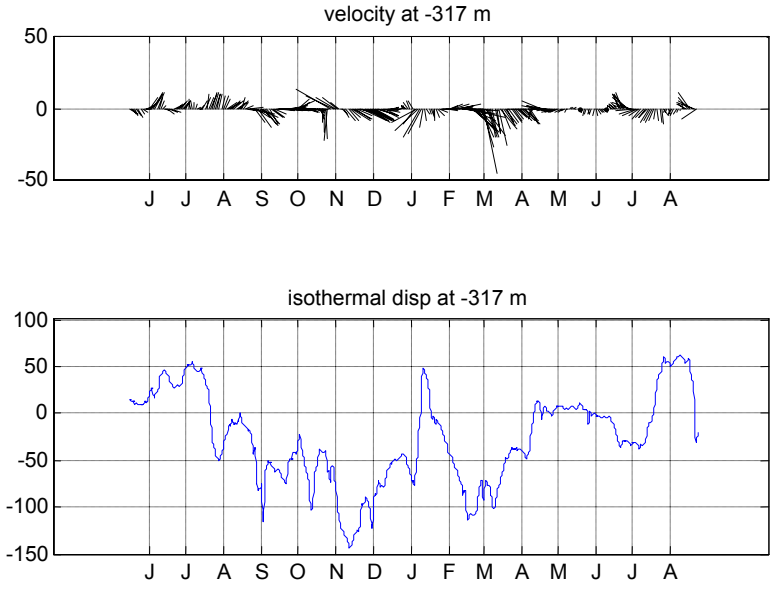

Figure 27a. Velocity vector (North component up page and East to the right) time series at the mooring location together with the associated isothermal vertical displacements at the depth level of 317 m. Time axis shows June to December, 2003 and January to August, 2004.

(b)

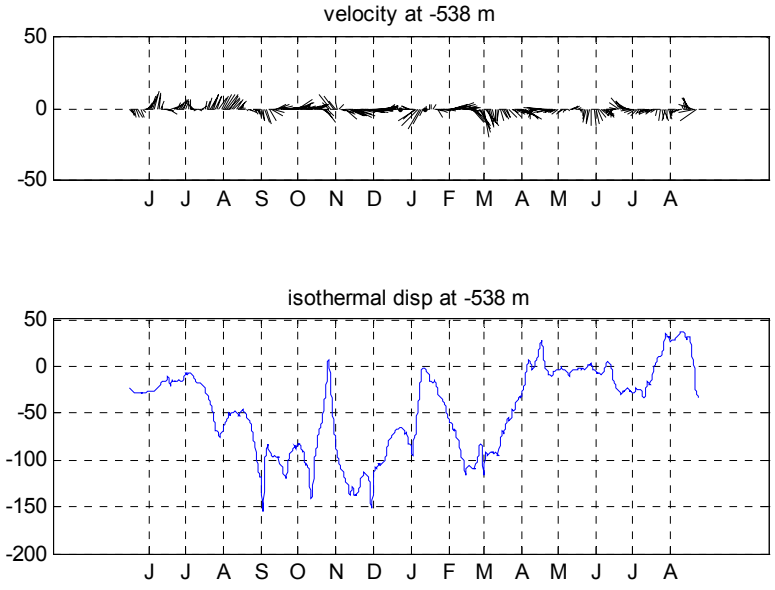

Figure 27b. As Figure 27a but at 538 m.

(c)

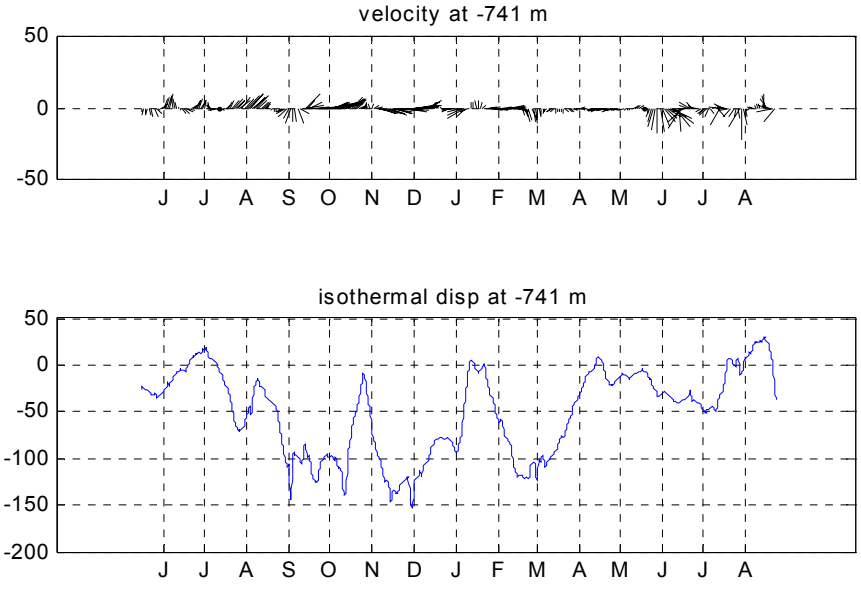

Figure 27c. As Figure 27a but at 741 m.

(d)

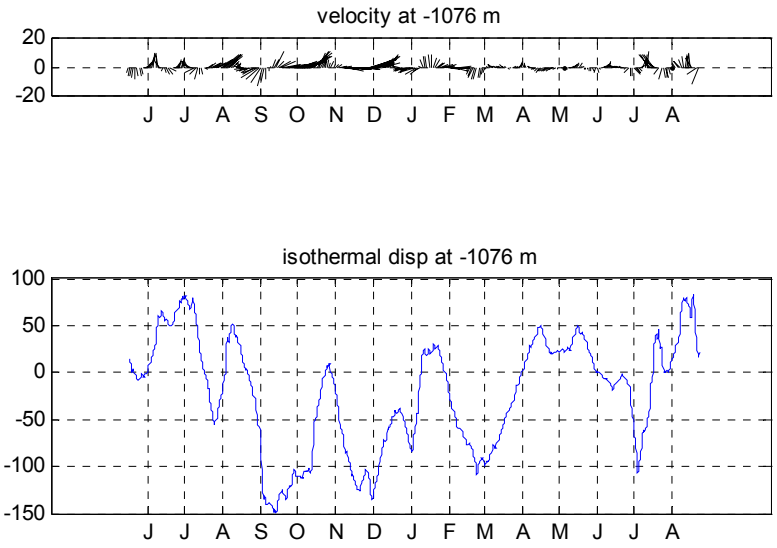

Figure 27d. As Figure 27a but at 1076 m.

(e)

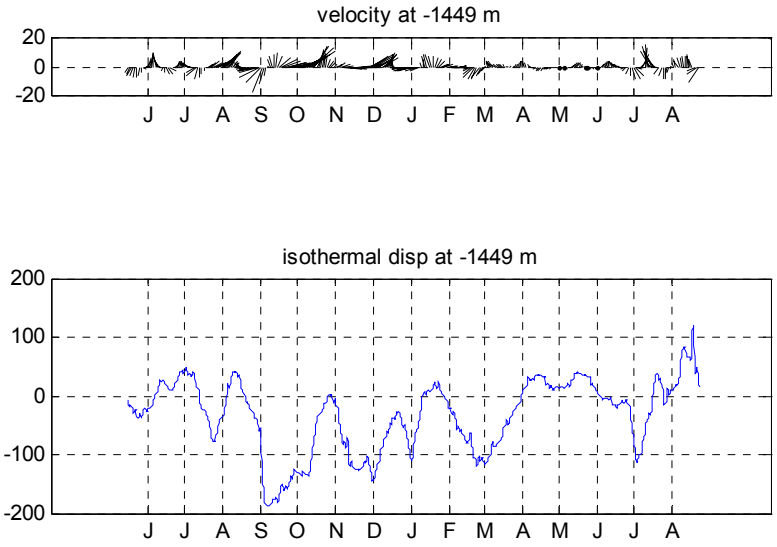

Figure 27e. As Figure 27a but at 1449 m.

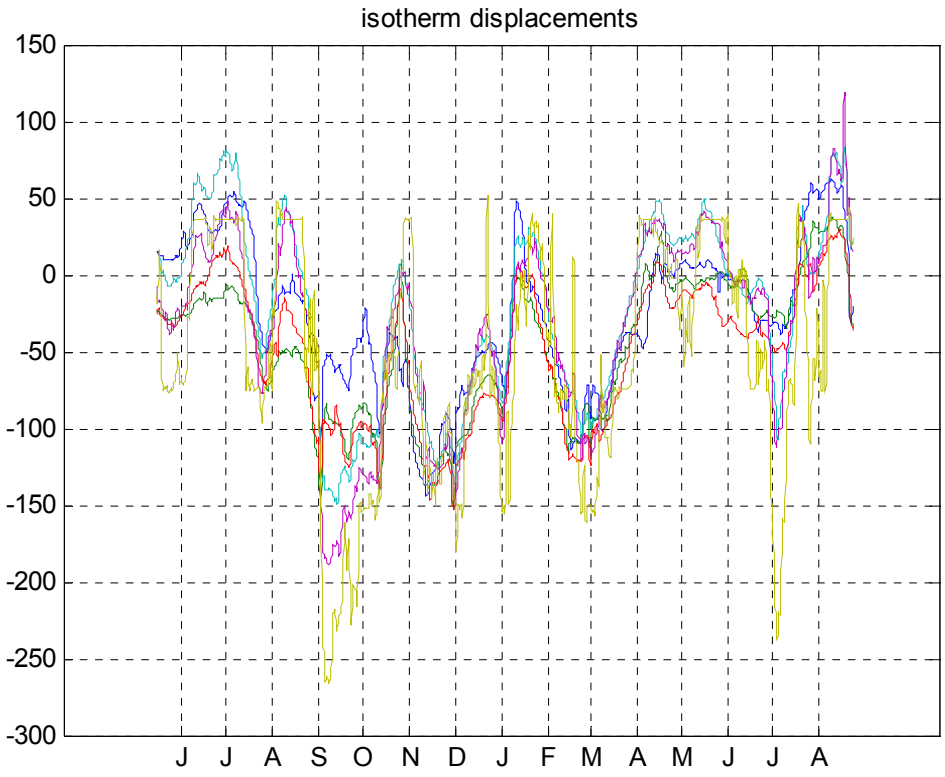

Figure 28. Isothermal vertical displacements down to 1500 m.

Figure 29 shows velocity hodographs corresponding to the periods in which the TEd and MEd eddies were close or over the mooring. Color-coding is done according to the potential temperature at each depth. Closed loops composed of warm waters coincide with the period when altimetry suggests the eddies were close or right at the mooring.

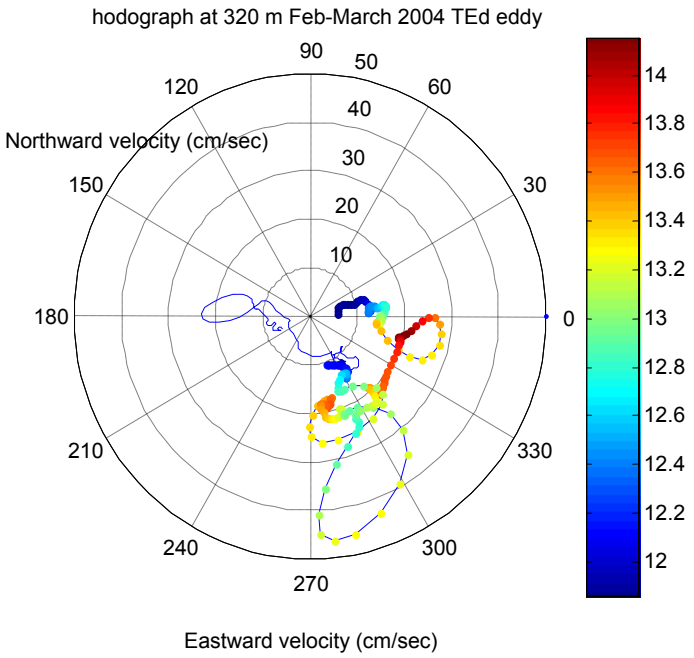

Figure 29a. Velocity hodographs corresponding to 320 m and the period in which the TEd eddy was close or over the mooring. Color-coding is done according to the potential temperature at each depth.

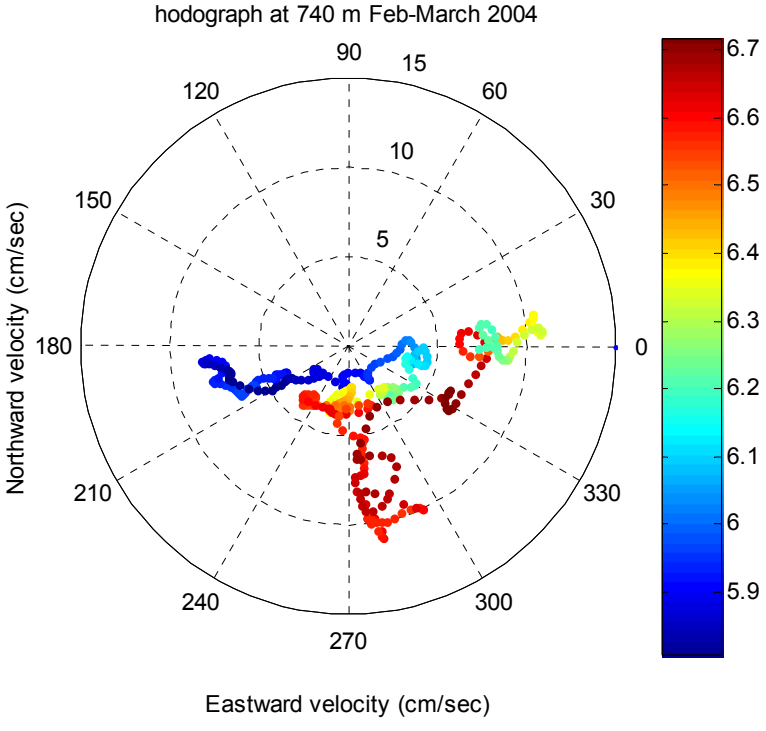

Figure 29b. As Figure 29a for 740 m.

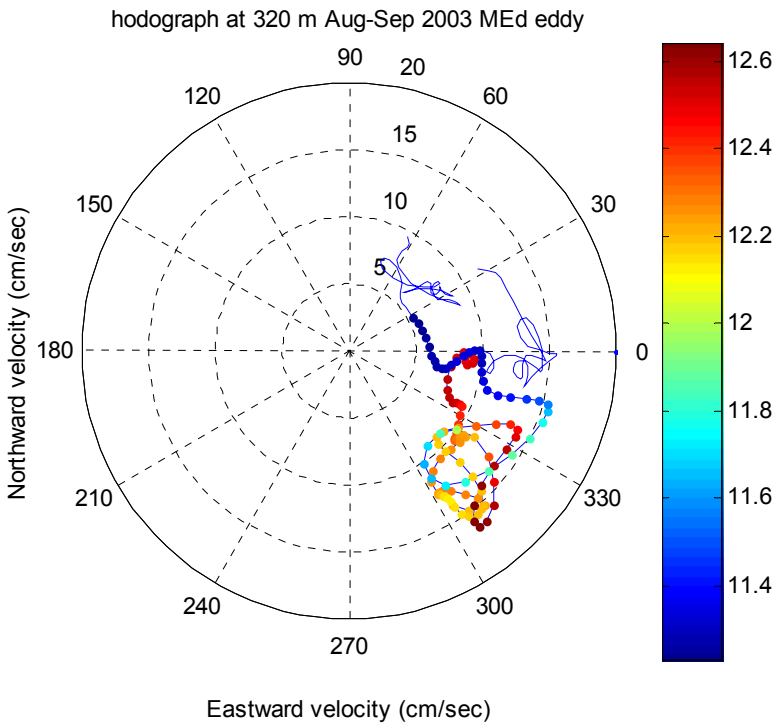

Figure 29c. As Figure 29A but for MEd eddy.

The final example of the correlation between the mooring measurements and satellite altimetry is shown in Figure 30. Panels in Figure 30a shows the absolute geostrophic velocity vector from AVISO analysis using a mean sea level computed from the GRACE satellite and surface drifters (Maximenko and Niiler, 2004) (top panel) and the mooring velocity vectors (low-passed) at 27 m depth (lower panel). Notice the difference in the horizontal time-axis in the figures, the high correlation between these independent observations is striking.

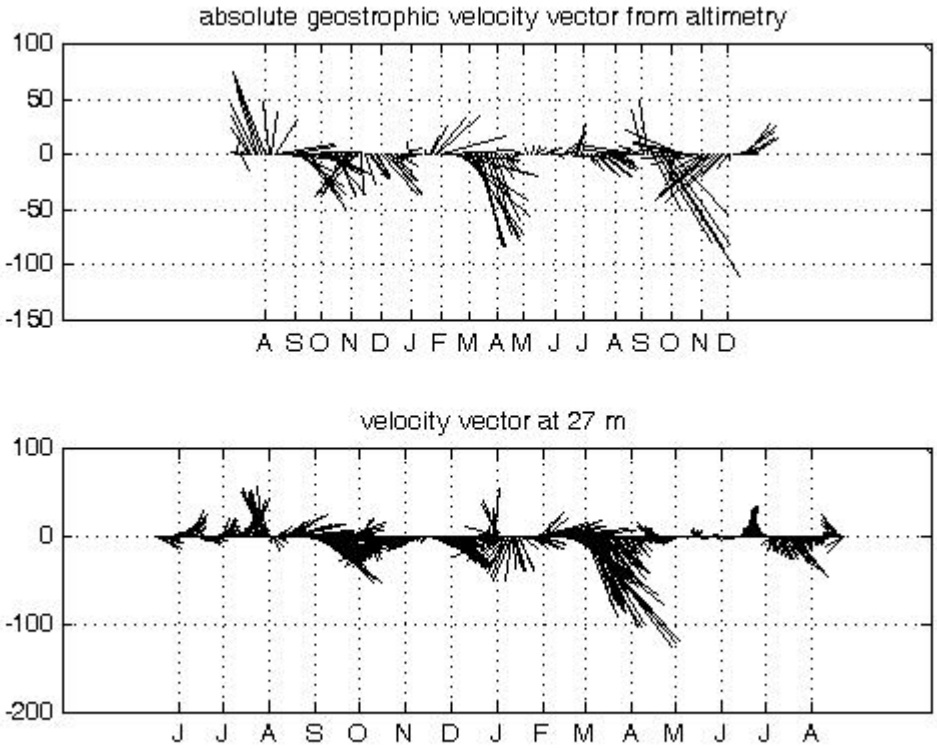

Figure 30. Absolute surface velocity vector from the Aviso Anlaysis (upper panel) and observed velocity at 27 meters depth (lower panel). Notice the difference in the time axis (horizontal) between the panels.

Although the high frequency near-inertial motions have a small contribution in terms of the velocity variance, they are a prominent feature in the time series. The spectral peak around the inertial period, in this latitude 28.22 h, is a common feature in oceanic observations. A classical and nowadays common procedure to analyze near-inertial motions is via complex demodulation (Pollard, 1970). The mean amplitude, as derived by demodulation, at three near surface depths and as a function of frequency in a near-inertial band shows the occurrence of near-inertial burst (Figure 31). The mean amplitude decreases with depth and away from the inertial frequency. That the peak is found at lower frequencies than the inertial has been explained by the existence of large scale flow vorticity, implying free internal wave motions superimposed in a flow field with planetary and flow anticyclonic vorticity that add up. In essence, the linear dynamics of perturbations superimposed on such background are influenced by an equivalent Coriolis parameter, which is the sum of the planetary and background vorticities. But the striking coincidence is the near-inertial intensification during the passage of frontal features associated with eddies. The events of MEd (in September, 2003), SEd (in November, 2003), TEd (in January and February, 2004) and UEd (in 2004) as just described at the beginning of this Section have a direct counterpart in the intensification of near-inertial motions (Figure 31).

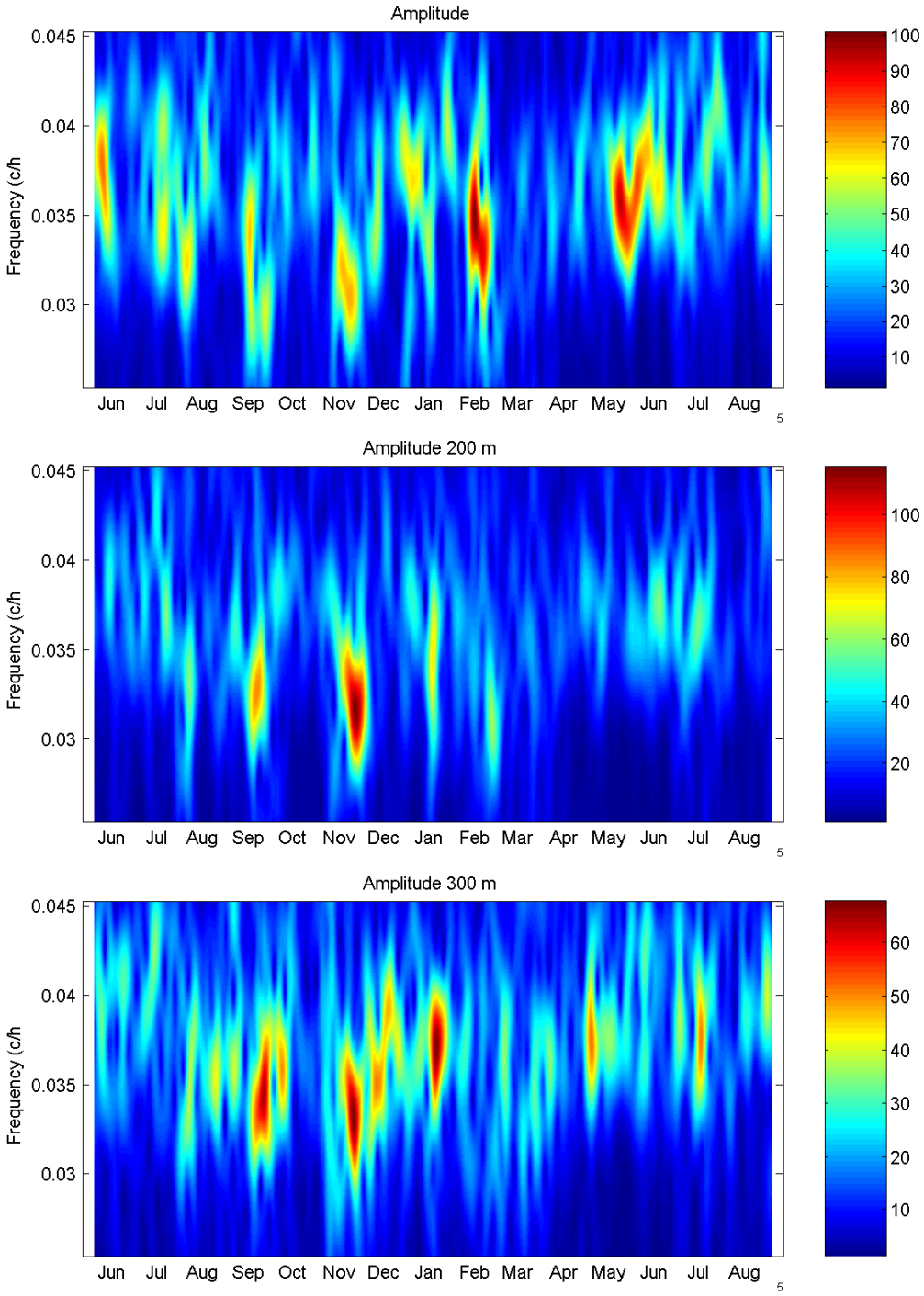

Figure 31. Amplitude in mm/s of near-inertial motions as a function of time and frequency for the depths of 100, 200 and 300 m. The inertial frequency is .0354 c/h, but the bursts occur centered at lower and higher frequencies. The increase in amplitude in September, 2003, November, 2003, January, 2004, and April, 2004 coincide with the passage of MEd, SEd, TEd, and UEd eddies.

6. Conclusions

A successful deployment of a highly instrumented deep mooring in the central Gulf of Mexico was carried out. Most of the instruments performed adequately and data recovery was highly successful. There were however some slight problems with a couple of instruments. For example, the mid-water LR-ADCP (75 kHz) had problems with the first few bins close to the head's instrument. Although all the data passed RDI's data quality tests by far, the above mentioned bins provided data which had no correlation with the bins above and relatively low velocity variance, and therefore were discarded. We are still looking on the cause of this malfunction. In addition, the 300 kHz ADCP located close to the bottom provided good data only for the first five bins due to the lack of sufficient reflectors farther away from the bottom.

Analysis of the velocity data shows that tides (diurnal components) and inertial oscillations have a relatively small contribution to the variability. Energy spectra are red, and most of the energy is in the subinertial motions. The 20-100 days period band is highly energetic. Particularly interesting is the fact that energy in the peak centered at periods around 30 days is larger at the bottom than the rest of the water column (except near surface). Mean velocity values are smaller than their standard deviations through the whole water column; energy is dominated by fluctuations rather than the mean currents. These fluctuations are related to the passage of eddies generated or related to Loop Current processes. Decomposition in dynamical modes and empirical orthogonal functions shows that 90% of the variability is explained by the barotropic and first baroclinic modes with energy nearly equipartitioned between them. Four EOFs are required to explain the same amount of velocity variance. Their structure varies depending on the way they are computed (see Section 3.2) and highlights the need to interpret the results with caution and the necessity of performing both statistical and dynamical decompositions to better interpret the results.

A new method is developed to correct mooring motion and determine temperature values at nominal instrument depths or any depth using the mooring measurements and a reference profile determined from CTD casts or climatology. The method is based on assuming adiabatic displacements of the reference profile and using potential temperature as a Lagrangian Label. The method appears to give similar results as other techniques available in the literature and its implementation is somewhat easier (Section 4). Comparison of mooring measurements with altimetry data for the same period shows that most energetic events are associated with eddies passing close or over the mooring. The high correlation between both sources of observations permits identification of the vertical penetration and time evolution of the anomalies identified by the altimeter data and gives confidence on the quality of the measurements. It is remarkable that eddies generate coherent detectable signals in velocity and isotherm displacements down to 1500 m depth, as can be seen from Figures 27 to 29.

The northeastward mean velocity and its variance measured in the mooring below 1000 m depth is consistent with the deep flow characteristics found in nearby regions using PALACE floats (Weatherly et al. 2005, DeHaan and Sturges 2005). For completeness we redraw the figure from Hamilton, 1990 which shows the deep circulation in the Gulf estimated from mooring measurements, adding the velocity vector (in blue) corresponding to our measurements:

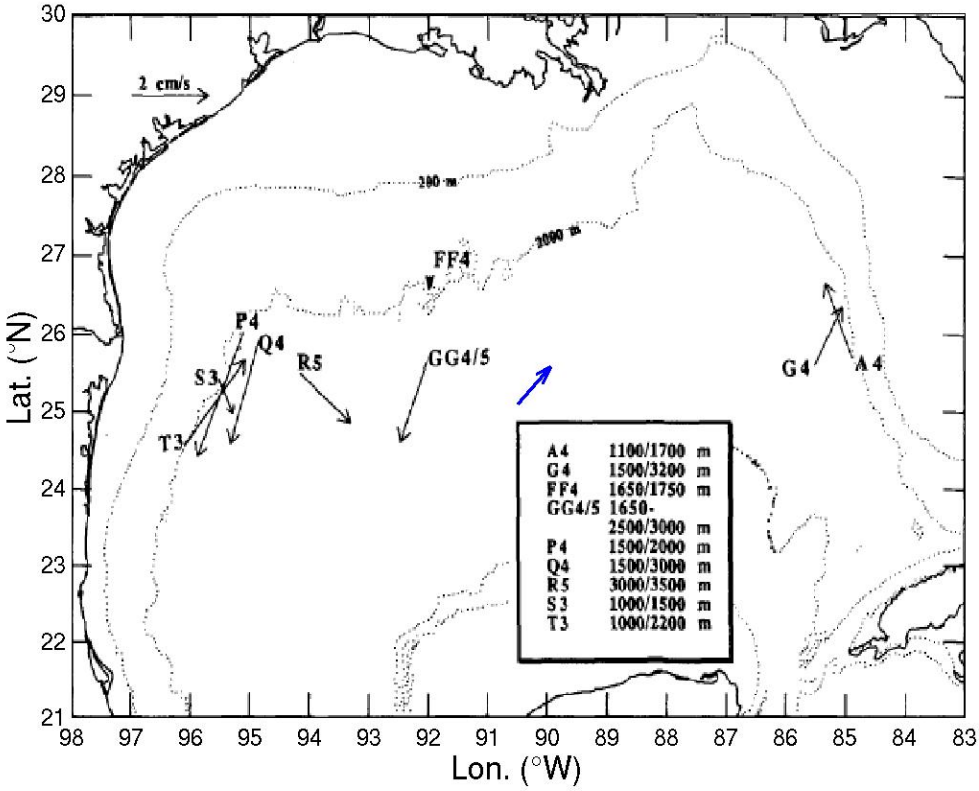

Figure 32. Deep mean circulation in the Gulf of Mexico, taken from Hamilton, 1990, including results of these measurements (blue arrow).

This mean is above noise level (small standard error) but given the large variability in the region, longer term measurements are required to determine its significance.

Perhaps the most remarkable finding of this study is the fact that data together with its dynamical and empirical modal decompositions suggest highly coherent motion throughout the water column which to a large extent can be decomposed into a barotropic and first baroclinic mode structure. Progressive vector diagrams and vector plots suggest an upper layer from the surface down to 800-900 meters depth, a transition layer between 900-1200 meters, more in tune with the upper layer, and a deep coherent layer below 1200 meters. This partition is consistent with the thermodynamic studies of Rivas et al., 2005, 2006 and the analysis of the deep circulation in the Caribbean and Gulf of Mexico of Sturges, 2005. The highly coherent motions below 1000 m, their bottom intensification and spectral characteristics are definitely reminiscent of Topographic Rossby waves, as found by Hamilton. However, further studies are necessary to corroborate this result.

7. References

Chassignet, E. P., H. E. Hurlburt, O. M. Smedstad, C. N. Barron, D. S. Ko, R. C. Rhodes, J. F. Shriver, A. J. Wallcraft, and R. A. Arnone. 2005. Assessment of data assimilative ocean models in the Gulf of Mexico using ocean color. In W. Sturges and A. Lugo-Fernández, editors. *Circulation in the Gulf of Mexico: Observations and Models*. AGU Monograph No. 161:87-100.

Chereskin, T. K., E. Firing, and J. A. Gast. 1989. Identifying and screening filter skew and noise bias in Acoustic Doppler Current Profiler measurements. J. Atmos. Oceanic Technol., 6:1040-1054.

Chérubin, L. M., W. Sturges, and E. P. Chassignet. 2005. Deep flow variability in the vicinity of the Yucatan Straits from a high-resolution numerical simulation. J. Geophys. Res., 110, C04009, doi:10.1029/2004JC002280.

DeHaan, C. J. and W. Sturges. 2005. Deep cyclonic circulation in the Gulf of Mexico. J. Phys. Oceanogr., 35(10):1801-1812.

Flagg, C. N. and S. L. Smith. 1989. On the use of the Acoustic Doppler Current Profiler to measure zooplankton abundance. Deep-Sea Res., 36:455-474.

Hamilton, P. 1990. Deep currents in the Gulf of Mexico. J. Phys. Oceanogr., 20:1087-1104.

Hamilton, P. and A. Lugo-Fernández. 2001. Observations of high speed deep currents in the northern Gulf of Mexico. Geophys. Res. Letters, 28(14):2867-2870.

Hogg, N.G. 1991. Mooring motion corrections revisited. J. Atmos. Oceanic Technol., 8(2):289-295.

Johns, W. E., T. J. Shay, J. M. Bane, and D. R. Watts. 1995. Gulf Stream structure, transport, and recirculation near 68°W. J. Geophys. Res., 100:817-838.

Leben, R. R. 2005. Altimeter-derived Loop Current metrics. In: W. Sturges and A. Lugo-Fernández, editors. *Circulation in the Gulf of Mexico: Observations and Models*. AGU Monograph No. 161:181-201.

Lohrmann, A., B. Hackett, and L. P. Røed. 1990. High resolution measurements of turbulence, velocity and stress using a Pulse-to-Pulse Coherent Sonar. J. Atmos. Oceanic Technol., 7:19-37.

Maximenko, N.A. and P.P. Niiler. 2004. Hybrid decade-mean global sea level with mesoscale resolution. In: N. Saxena, editor. *Recent Advances in Marine Science and Technology*. Honolulu: PACON International. Pp. 55-59.

Nowlin, W. D., Jr. and H. J. McLellan. 1967. A characterization of the Gulf of Mexico waters in winter. J. Mar. Res., 25:29-59.

Nowlin, W. D., Jr., D. F. Paskausky, and H. J. McLellan. 1969. Recent dissolved-oxygen measurements in the Gulf of Mexico deep waters. J. Mar. Res., 27:39-44.

Nowlin W.D., A.E. Jochens, S.F. DiMarco, and R.O. Reid. 2000. Physical oceanography. In: Continental Shelf Associates, Inc., editor. Deepwater Gulf of Mexico environmental and

socioeconomic data search and synthesis. Vol. 1: Narrative report. U.S. Depart. of the Interior, Minerals Management Service, Gulf of Mexico OCS Region, New Orleans, Louisiana. OCS Study MMS 2000-049. 360 pp.

Oey, L.-Y. and H.-C. Lee. 2002. Deep eddy energy and topographic Rossby waves in the Gulf of Mexico. J. Phys. Oceanogr., 32:3499-3527.

Pollard, R.T. 1970. On the generation by wind of inertial waves in the ocean. J. Mar. Res. 17:795-812.

RD Instruments. 1998. ADCP coordinate transformations. formulas and calculations. RDI Tech. Manual P/N 951-6079-00. 26 pp.

Ripa, P. 1981. Symmetries and conservation laws for internal gravity waves. In: B.J. West, editor. Nonlinear Properties of Internal Waves. AIP Conf. Proc., 76:281-306.

Ripa, P. 1990. Positive, negative and zero wave energy and the flow stability problem, in the Eulerian and Lagrangian-Eulerian descriptions. Pure Appl. Geophys., 133:713-732.

Rivas, D., A. Badan, and J. Ochoa. 2005. The ventilation of the deep Gulf of Mexico. J. Phys. Oceanogr., 35:1763-1781.

Rivas, D., A. Badan, J. Sheinbaum, J. Ochoa, and J. Candela. 2006. An upward heat flux in the central Gulf of Mexico. J. Phys. Oceanogr. (submitted).

Schmitz, W. J., Jr. 2005. Cyclones and westward propagation in the shedding of anticyclonic rings from the Loop Current. In: W. Sturges and A. Lugo-Fernández, editors. *Circulation in the Gulf of Mexico: Observations and Models*. AGU Monograph No. 161:241-261.

Schott, F. 1986. Medium-range vertical acoustic Doppler current profiling from submerged buoys. Deep-Sea Res., 33:1279-1292.

Schott, F. and W. Johns. 1987. Half-year-long measurements with a buoy-mounted Acoustic Doppler Current Profiler in the Somali Current. J. Geophys. Res., 92:5169-5176.

Schott, F. 1988. Effects of a thermistor string mounted between the acoustic beams of an Acoustic Doppler Current Profiler. J. Atmos. Oceanic Technol., 5: 154-159.

Sturges, W. 2005. Deep-water exchange between the Atlantic, Caribbean and Gulf of Mexico. In: W. Sturges and A. Lugo-Fernández, editors. *Circulation in the Gulf of Mexico: Observations and Models*. AGU Monograph No. 161:263-278.

van Haren, H., N. Oakey, and C. Garrett. 1994. Measurements of internal wave band eddy fluxes above a sloping bottom. J. Mar. Res., 52:909-946.

Weatherly, G. L., N. Wienders, and A. Romanou. 2005. Intermediate-depth circulation in the Gulf of Mexico estimated from direct measurements. In: W. Sturges and A. Lugo-Fernández, editors. *Circulation in the Gulf of Mexico: Observations and Models*. AGU Monograph No. 161:315-324.

The Department of the Interior Mission

As the Nation's principal conservation agency, the Department of the Interior has responsibility for most of our nationally owned public lands and natural resources. This includes fostering sound use of our land and water resources; protecting our fish, wildlife, and biological diversity; preserving the environmental and cultural values of our national parks and historical places; and providing for the enjoyment of life through outdoor recreation. The Department assesses our energy and mineral resources and works to ensure that their development is in the best interests of all our people by encouraging stewardship and citizen participation in their care. The Department also has a major responsibility for American Indian reservation communities and for people who live in island territories under U.S. administration.

The Minerals Management Service Mission

As a bureau of the Department of the Interior, the Minerals Management Service's (MMS) primary responsibilities are to manage the mineral resources located on the Nation's Outer Continental Shelf (OCS), collect revenue from the Federal OCS and onshore Federal and Indian lands, and distribute those revenues.

Moreover, in working to meet its responsibilities, the **Offshore Minerals Management Program** administers the OCS competitive leasing program and oversees the safe and environmentally sound exploration and production of our Nation's offshore natural gas, oil and other mineral resources. The MMS **Minerals Revenue Management** meets its responsibilities by ensuring the efficient, timely and accurate collection and disbursement of revenue from mineral leasing and production due to Indian tribes and allottees, States and the U.S. Treasury.

The MMS strives to fulfill its responsibilities through the general guiding principles of: (1) being responsive to the public's concerns and interests by maintaining a dialogue with all potentially affected parties and (2) carrying out its programs with an emphasis on working to enhance the quality of life for all Americans by lending MMS assistance and expertise to economic development and environmental protection.